Electron-skyrmion systems, in and out of equilibrium, and isolated or contacted to reservoirs

Emil Östberg

LUNDS UNIVERSITET

Supervisors: Emil Viñas Boström and Claudio Verdozzi

Thesis submitted for the degree of master (60 hp)

Department of Physics
Division of Mathematical Physics

Acknowledgments

First, I would like to express my deepest gratitude to Claudio and Emil, who guided me throughout this project. During this time, I have learned lots of condensed matter physics, both within the scope of the project and outside. Their knowledge of the field and intuition, and their theoretical and computational advice always guided the project in the right direction. Without their unyielding support, this project would have turned out to be different from what it is now. Towards the end of the project, they also helped me a lot with comments and suggestions about the thesis, much more than I expected, and I appreciate this a lot.
I would then like to acknowledge my officemates: Francesco, Zackaria and Daniel, who have been pleasant company for the whole time and the source of deep discussions within and outside science. And, finally, I wish to thank my family and friends outside physics, who have shown their support through this thesis work.

Abstract

A Kondo lattice skyrmion model in contact with a macroscopic environment is simulated to explore skyrmion dynamics, which is an extension of previous work [1, 2]. The system is simulated using non-equilibrium Green's functions within the generalized Kadanoff-Baym ansatz and the wide band limit. To get a time-linear scaling, we present an approximation to the collision integral, which offers a good trade-off between computation time and accuracy. We find a new regime of skyrmion dynamics when the current from the macroscopic environment is sufficiently high, and the effect of impurities is explored. Furthermore, an analysis of the itinerant conduction electrons shows that a nontrivial topology is present when a skyrmion is present.

Contents

List of abbreviations

GF - Green's function
NEGF - Non-equilibrium Green's function
DFT - Density functional theory
DMI - Dzyaloshinskii–Moriya interaction
WBL - Wide band limit
GKBA - Generalized Kadanoff-Baym ansatz
DOS - Density of states
LDOS - Local density of states
RHS - Right hand side
LHS - Left hand side
CM - Center of mass

CHAPTER 1

Introduction and Theory

1 Introduction

The governing equation of quantum mechanics is the Schrödinger equation: it prescribes how the wavefunction propagates through time. The wave function is the quantity usually needed to calculate the probabilities of outcomes in experiments. As physical systems become smaller, a quantum description is necessary. The classical description is then no longer complete. Today electronic devices are at the scale where quantum effects start to appear and nano-scale systems have become all the more important in research and society. Hence, there is an immense need to solve the Schrödinger equation in such contexts.
Nevertheless, simulating nano-scale devices from first principles is a significant challenge of modern physics since the calculations complexity grows rapidly with the number of particles. It is especially difficult if the particles interact; when there are multiple interacting quantum particles, this becomes a many-body problem. Even if one could solve the many-body problem to get the full many-body wave function, it would not be of practical relevance since it contains too much information. Therefore often reduced quantities are calculated, for example two particle correlation functions. Such functions can then be related to the physical quantities of interest since almost all physical quantities can be described by two-particle correlation functions. Another route is to simplify the problem by considering one particle at a time. If the particles are not interacting: this is in fact several one-particle problems. Such problems have a known solution which has the mathematical form of a matrix determinant, called a Slater determinant if one is considering fermionic particles (for bosonic particles the solution is a permanent rather than a determinant).
A great advance in the field of many-body theory came during the 1960s with Density functional theory (DFT) [3, 4]. DFT provides an exact mapping between an interacting many-body problem to multiple non-interacting problems, and as previously mentioned a single particle problem is easier to solve than an interacting problem. However, often the central quantity in DFT, called the exchange correlation potential, is very difficult to compute

without making approximations. This limits in an important way the phenomena DFT can describe.

Traditionally strongly correlated materials have been out of the reach of DFT, both in and out of equilibrium. Green's function techniques are considered the natural way to proceed. The Green's function (GF) is a correlation function between two points in space and time, so one expects no correlation between points with a large separation and thus the GF vanishes for two distant points in space-time. Contrary to the GF, the one-particle wave function that is used in some DFTs only depends on one position in space and time. In GF theory, the central quantity is called the self-energy, which technically is an integral kernel and therefore it is a function of two points in space and time. We will be dealing with Non-equilibrium Green's functions (NEGF). The equilibrium counterpart is a special case of NEGF, where the Hamiltonian is time-independent. Often, pure NEGF is not used since the two-time scheme necessitates a cubic computation time as a function of the number of time-steps. A standard approximation is the generalized Kadanoff Baym ansatz (GKBA), where the two-time scheme is replaced by a single-time scheme for the one-particle density matrix, and then one gets quadratic computation time. In this thesis, NEGF with GKBA will be used to simulate the time evolution of a system from its initial preparation.

We will focus on a setup that is close to an experimental scenario: a central system in contact with an environment. The environment is modeled as metallic leads where a bias can be applied, which allows us to address quantum transport. The electrons in the leads are free to move as in a metal, thus they act as a source and a drain to (de)stabilize the electrons in the system. The environment introduces an extra term in the collision integral, called embedding self-energy. A common problem in NEGF+GKBA is the appearance of quadratic computation time due to the collision integral. The collision integral is complicated due to the integral kernel, i.e. the aforementioned self-energy. For our purposes, the self-energy includes the effects of the metallic leads. However, in general, many-body interactions also contribute to the self-energy.

Recently a scheme called G1-G2 was proposed to deal with the collision integral, which was a significant advance in the field of NEGF [5]. The G1-G2 scheme yields a time-linear scheme for many-body self-energies. Nonetheless, it is not clear how to apply the G1-G2 scheme for self-energies coming from leads, called embedding self-energies.

A scheme was proposed in [6] where the collision integral is approximated by doing a Padé approximant of the Fermi-function, which yields a time-linear scheme even for embedding self-energies. The scheme is time-linear, and later in the next chapter (section 1.6) we will see that still 40-80 quantities need to be evaluated at every time-step.

In this work, since we treat large central magnetic regions and perform time propagation to rather long times, we consider a non-interacting approximation to the collision integral. While approximate, this prescription retains the linear time scaling but requires a maximum of only two quantities to be evaluated at each time step. As shown later, our approximate scheme provides a reasonable trade-off between computation time and accuracy.

The aim of this thesis is to simulate skyrmions in lattice models, where the Hamiltonian used was introduced in previous work [1] and can be derived from a two-band s-d model [2]. A lattice model is a model that lives on a discrete set of points: instead of simulating a continuous space, one can restrict the simulation to discrete lattice sites. This is motivated by the physical scenario that one is faced with in a solid, where atoms are bound together

to form a periodic structure. The discrete set of points then corresponds to the orbits of the atoms, where electrons can reside. Lattice models are used extensively in condensed matter theory. An early example of this type of model is the Ising model where there is a spin at every lattice site and the spins can only be up or down. The spins interact between nearest neighbours such that they gain energy when nearest neighbour spins are not aligned, if we assume ferromagnetic coupling. To minimize the energy, all spins want to align in one direction, which gives rise to a ferromagnetic order in the lattice. One could also consider anti-ferromagnetic coupling, promoting a state where the spins are misaligned. Despite its simplicity, the Ising exhibits a phase transition at a critical temperature T_c between an ordered and a disordered state, called an order-disorder transition.

A more faithful representation of the localized moments in a solid is given by the Heisenberg model, where the moments can point in any direction. The interaction between moments is through an exchange interaction, which also favors alignment when we have ferromagnetic coupling. The exchange interaction is a manifestation of the antisymmetry of electrons, and responsible for ferromagnetic order in real materials. In addition, many materials exhibit also an antisymmetric form exchange, called Dzyaloshinskii–Moriya interaction (DMI) which favors orthogonal alignment between moments. The symmetric exchange is mathematically a dot product and the antisymmetric exchange is a cross product, therefore the magnitude is given by $\cos(\theta)$ and $\sin(\theta)$ respectively, where θ is the angle between the two spins which interact. The $\sin(\theta)$-function is anti-symmetric and the $\cos(\theta)$-function is symmetric, hence the DMI vanishes when the lattice is symmetric with respect to a fixed point i.e. in the presence of inversion symmetry.

The localized moments do not tell the whole story, since often the localized moments coexist within a sea of itinerant electrons (one can for example think of localized magnetic moments originating from unfilled f-shells, which coexist with itinerant (s-p) and more localized (d-) electrons). A most striking example is provided by the Kondo effect, which occurs when one decreases the temperature in a metal and measures the resistivity. From Fermi-liquid theory, one expects a quadratic decrease, but experiments showed that the resistivity of the metal stops decreasing after a certain point and starts instead to increase giving rise to a resistance minimum [7]. The Kondo model was introduced to explain this phenomenon and it describes a single localized moment coupled via exchange interactions to the spins of a sea of itinerant (conducting) electrons. Kondo showed that this model gives rise to a minimum in the resistance as a function of temperature, due to the renormalization of the coupling constant at low temperatures. Even though a resistance minimum was found, a new problem arose: the coupling constant diverged at zero temperature. This issue was long a problem in condensed matter physics, until it was solved in the 1970s by Wilson using renormalization group techniques [8]. The Kondo model is analytically tractable, but one needs to complicate the picture further to go further toward realistic systems. In principle every lattice site could have a localized moment, and this is precisely the scenario to be considered in this thesis, namely a Kondo lattice where the localized spins also experience the Dzyaloshinskii–Moriya interaction.

A cubic B20 MnSi compound could be considered a Kondo lattice, since experimentally one has found localized moments at every site and there are bands that indicate the presence of conduction electrons [9]. B20 is a classification of the crystal structure and there is a corresponding symmetry group. MnSi is expected to have a competition between localized

moments and free electrons due to the d-orbital character of Mn and the p-orbital character of Si. Nonetheless, B20 MnSi is far from completely understood. Due to its lack of inversion symmetry and non-Fermi liquid behaviour it has gained attention in recent years. It was in fact, in B20 MnSi that magnetic skyrmions first were observed experimentally [10]. Only later on magnetic skyrmions were also found in many other compounds with broken inversion symmetry.

Magnetic skyrmions are topological excitations that are stabilized from the competition between Dzyaloshinskii–Moriya interaction (DMI) and the ordinary Heisenberg exchange interaction [11]. Consider a two-dimensional lattice with these two interactions. The DMI wants the spins to form a $\pi/2$ radians angle, and if we only have DMI interaction, then four spins in a square would form a full loop due to them being orthogonal to each other. However, we also have the exchange interaction that promotes the spins to develop a 0 radians angle, which means that the favored angle for the moments is somewhere in between 0 and $\pi/2$ radians. Such energy balance gives rise to the magnetic vortices, called magnetic skyrmions, which are observed in for example B20 MnSi.

Magnetic skyrmions have recently garnered attention, since one can create memory devices using skyrmions, called race track memories [12]. A race track memory is a device containing a long magnetic stripe, the "racetrack". The racetrack is divided up into cells, where there is either a single skyrmion or no skyrmion at all and this is what gives either a zero or a one. These cells are not divided by a physical barrier, instead there is a confining potential at every cell. A physical barrier could cause the skyrmions to annihilate. A possibly more effective experimental realization is to have skyrmions or antiskyrmions in each cell, for example a skyrmion is a one and a antiskyrmion is a zero. One then applies a magnetic field to flip the skyrmion into an antiskyrmion, and uses the opposite field to flip an antiskyrmion into a skyrmion. To achieve high-quality racetrack memories, one must create and destroy skyrmions with high precision. Furthermore, the movement of the skyrmion is crucial to understand, since in some racetrack memories, the idea is to move skyrmions along the racetrack. Finally, small impurities in the racetrack could annihilate the skyrmion and it is key to understand how pure the racetrack must be.

In this thesis we will address these questions by developing a new approach to transport in skyrmion systems, by considering a non-interacting approximation to the NEGF+GKBA collision integral. We will investigate the role of electronic currents and magnetic impurities on the motion of skyrmions using the new method. This will also allow us to study some of the properties of the itinerant electrons, an aspect that so far has virtually received no attention in the literature.

2 Theory

2.1 Emergence of antisymmetric exchange

Antisymmetric exchange is a consequence of superexchange in the presence of spin-orbit interaction, where superexchange is the exchange interaction of ions through an intermediate atom. For example, in MnO the Mn atoms are not directly bonded, hence they are not expected to interact through exchange. Nevertheless, an exchange interaction is present which is mediated by the oxygen atom. Strictly speaking, it is not necessary to have an intermediate atom for antisymmetric exchange, but it is often the case. The authors in [2] showed that antisymmetric exchange could be derived in a single-band Hubbard model with spin-orbit coupling. The exchange interaction can be understood for two isolated electrons as a consequence of the total wavefunction being antisymmetric. It is energetically favorable for the electrons to have a spatially antisymmetric wavefunction, since that minimizes the wavefunction overlap and, therefore the Coulomb repulsion between them. Since the spatial part is antisymmetric and the total wavefunction is also antisymmetric, the spin part is forced to be symmetric. Effectively there is an interaction $-J\mathbf{S}_1 \cdot \mathbf{S}_2$ ($J > 0$) which favors parallel alignment of the spins, where $J > 0$ is aforementioned ferromagnetic coupling which promotes ferromagnetic ordering in the solid. We could also have anti-ferromagnetic coupling $J < 0$, favoring anti-alignment, which would produce an ordering where the spins flip at every lattice site. For more than two particles, the situation is much more complicated, even more so when the exchange is mediated by an intermediate atom and spin-orbit coupling is present.

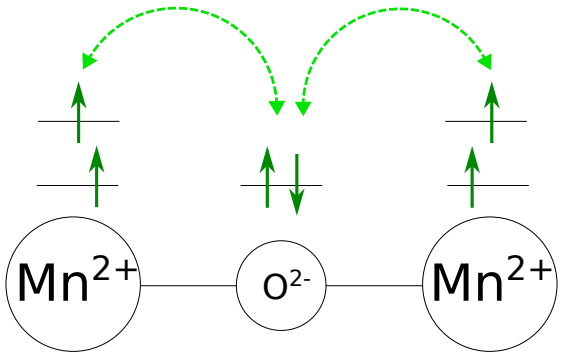

Figure 1.1: MnO structure. The energy levels for the two outermost valence electrons of Mn^{2+} ([Ar]$3d^5$) and O^{2-} ([He]$2s^2 2p^2$) are drawn schematically.

The original derivation of antisymmetric exchange by Moriya [13] was based on Anderson's theory of superexchange [14]. At the time Moriya strongly suspected there to be an antisymmetric exchange since two years prior Dzyaloshinskii had provided a phenomenological theory for α-Fe_2O_3 where an antisymmetric exchange appeared. However, we will give a more modern discussion based on [15]. Consider a general Hamiltonian for a lattice containing two types of atoms, where one has p-type (the O) orbitals, and one has d-type (the Mn) orbitals as in Fig. 1.1

$$H = \sum_{jm\sigma} \epsilon_m d^\dagger_{jm\sigma} d_{jm\sigma} + \sum_{kn\sigma} \varepsilon_n p^\dagger_{kn\sigma} p_{kn\sigma} + U \sum_{jmm'} d^\dagger_{jm\uparrow} d^\dagger_{jm'\downarrow} d_{jm'\downarrow} d_{jm\uparrow} + \sum_{\langle jk\rangle mn\sigma} (V_{jm,kn} d^\dagger_{jm\sigma} p_{kn\sigma} + h.c.) + \lambda \sum_j \mathbf{L}_j \cdot \mathbf{S}_j, \tag{1.1}$$

$\langle jk \rangle$ signifies summation over nearest neighbour sites, $d^\dagger_{jm\sigma}$ ($d_{jm\sigma}$) is the creation (annihilation) operator for a d-electron in the m-th orbital on the j-th site with spin σ, $p^\dagger_{jm\sigma}$ ($p_{jm\sigma}$) is the creation (annihilation) operator for a p-electron in the m-th orbital on the j-th site with spin σ, ϵ_m is the energy levels of the d-orbitals, ε_n is the energy levels of the p-orbitals, U is the Coulomb repulsion, λ is the spin-orbit interaction on the d-orbitals and $V_{jm,kn}$ is the amplitude for an electron to jump from the site k to j and orbital n to m. The indices j and k run over lattice sites, indices m, m' and n run over orbitals and σ is the spin of the orbitals. We now project the Hamiltonian on the low energy subspace which only contains the lowest orbital in Mn, mathematically one can do a first-order perturbation calculation in λ since $\hat{\mathbf{L}}_j \cdot \mathbf{S}_j = \hat{L}_{j,z}\hat{S}_{j,z} + \frac{1}{2}(L_{j,+}S_{j,-} + S_{j,+}L_{j,-})$ is what mixes the orbitals [15, 16].

$$H_{eff} = \sum_{kn\sigma} \varepsilon_k p^\dagger_{kn\sigma} p_{kn\sigma} + U \sum_j d^\dagger_{j0\uparrow} d^\dagger_{j0\downarrow} d_{j0\downarrow} d_{j0\uparrow} + \sum_{\langle jk \rangle mn\sigma} (V_{j0,kn} d^\dagger_{j0\sigma} p_{kn\sigma} + h.c.) \tag{1.2}$$

$$+ \sum_{\langle jk \rangle n} \sum_{\alpha\beta} \mathbf{C}_{jkn} \cdot (d^\dagger_{j0\alpha} \boldsymbol{\sigma}_{\alpha\beta} p_{nk\beta} + h.c) \qquad \mathbf{C}_{jkn} = -\frac{\lambda}{2} \sum_m \frac{\mathbf{L}^*_{jm0}}{\epsilon_m} V_{jm,kn} \tag{1.3}$$

We get a new term where the spin can flip when hopping from Mn to O and vice versa, which is the only effect of the spin-orbit interaction left. We now have a simpler Hamiltonian which has a strange type of hopping term.
To understand the exchange interaction we take a slight detour into a simpler model called the Hubbard model:

$$H_{Hub} = V \sum_{\langle jk \rangle \sigma} (d^\dagger_{j\sigma} d_{k\sigma} + h.c.) + U \sum_j d^\dagger_{j\uparrow} d^\dagger_{j\downarrow} d_{j\downarrow} d_{j\uparrow}, \tag{1.4}$$

which is a very simplified version of the Hamiltonian above. Furthermore, the energy scale in the Hubbard model is U/V, this contains only one species of particle and one orbital. In the limit of large Coulomb repulsion U/V, the electrons get localized on lattice sites. If we are at half-filling, there will be one electron per lattice site, since double occupancy is penalized by an energy U. One can perform a second-order perturbation theory calculation to find an effective Hamiltonian [17]

$$J \sum_{\langle jk \rangle} \mathbf{S}_i \cdot \mathbf{S}_j, \tag{1.5}$$

where $J = 4V^2/U$ is the exchange interaction, $\mathbf{S}_i = \sum_{\alpha\beta} d^\dagger_{i\alpha} \boldsymbol{\sigma}_{\alpha\beta} d_{i\beta}$ and $\boldsymbol{\sigma}_{\alpha\beta}$ is the components of the vector containing the Pauli matrices $(\sigma_x, \sigma_y, \sigma_z)$. It is crucial to consider half-filling, otherwise we get extra terms in the perturbation theory. As a matter of fact, this result was obtained already in Anderson's model of superexchange [14].
Inspired by the Hubbard model, we analyze the limit of small hopping, since this is the regime where the exchange interaction is expected to dominate. One should consider the fourth-order terms in $V_{j0,kn}$ with perturbation theory, since it takes four jumps for a hole to go from an Mn atom and back. We get the new term [13, 15]:

$$H_{ex} = J \sum_{\langle ij \rangle} \mathbf{S}_i \cdot \mathbf{S}_j + \sum_{\langle ij \rangle} \mathbf{D}_{ij} \cdot \mathbf{S}_i \times \mathbf{S}_j + \sum_{\langle ij \rangle} \mathbf{S}_i \overleftrightarrow{\Gamma}_{ij} \mathbf{S}_j. \tag{1.6}$$

J is the ordinary Heisenberg exchange, $\mathbf{D}_{ij} = -\mathbf{D}_{ji}$ is the DMI and $\overleftrightarrow{\Gamma}_{ij}$ is the tensor part where the arrows signify that dot-product should be taken to the left and the right. Moryia provided a simple estimate for the order of magnitude of these terms:

$$|\mathbf{D}_{ij}| \sim (\Delta g/g) J f_{ij} \qquad |\overleftrightarrow{\Gamma}_{ij}| \sim (\Delta g/g)^2 J h_{ij}, \tag{1.7}$$

where g is the gyromagnetic ratio in the solid, Δg is a deviation of the gyromagnetic ratio compared to a free electron, f_{ij} and h_{ij} ensure the correct site dependence. Within the estimate $|\overleftrightarrow{\Gamma}_{ij}|$ is the smallest, hence $\overleftrightarrow{\Gamma}_{ij}$ will not be considered in our calculations.

2.2 Spin dynamics

Most treatments of skyrmions are through purely classical equations, either the Thiele equation or the Landau-Lifshitz-Gilbert (LLG) equation [18, 19]. The LLG equation is given by

$$\frac{\mathrm{d}\mathbf{S}_i}{\mathrm{d}t} = -\gamma \mathbf{S}_i \times \mathbf{F}_i + \alpha \mathbf{S}_i \times \frac{\mathrm{d}\mathbf{S}_i}{\mathrm{d}t}, \tag{1.8}$$

here γ is the gyromagnetic ratio and α is the magnitude of the phenomenological Gilbert damping. If the spins were completely isolated, we would only have the first term, where $\mathbf{F}_i$ can include the forces from for example: Heisenberg exchange, DMI and external magnetic field. The second term dissipates energy such that the spins relax to the ground state after some time and can be imagined to come from e.g. lattice vibrations or a thermal bath. The LLG equation describes the movement of localized moments only, which is insufficient to analyze current-induced skyrmion transport. However, it is not clear how to incorporate current through the sample in simulations of the LLG equation, since free electrons are not simulated. Often the moments of itinerant electrons interact with the localized spins through a Kondo coupling

$$-g \sum_i \mathbf{S}_i \cdot \hat{\mathbf{s}}_i, \tag{1.9}$$

where g is the strength of the interaction, $\mathbf{S}_i$ is the classical spin on lattice site i simulated in the LLG equation and $\hat{\mathbf{s}}_i$ is the quantum spin of the itinerant electrons at site i. We will assume a positive coupling in this work, which promotes the alignment of the itinerant electrons with the localized moments. To derive an effective theory for only the localized moments, one assumes that there are itinerant electrons flowing through the system which are coupled to the moments through such a Kondo coupling, and the coupling is taken to infinity such that the moments align [20, 21]. One also needs to assume ballistic transport, furthermore the itinerant electrons are assumed non-interacting, and in such a scenario one can write the energy for the interaction by analogy. However, the analogy only holds to first-order in the magnetic potential. The result is the following approximate equation:

$$\frac{\mathrm{d}\mathbf{S}_i}{\mathrm{d}t} = -\gamma \mathbf{S}_i \times \mathbf{F}_i + \alpha \mathbf{S}_i \times \frac{\mathrm{d}\mathbf{S}_i}{\mathrm{d}t} + \frac{pa^3}{2e}(\mathbf{j} \cdot \boldsymbol{\nabla})\mathbf{S}_i - \frac{pa^3\beta}{2e}\mathbf{S}_i \times (\mathbf{j} \cdot \boldsymbol{\nabla})\mathbf{S}_i. \tag{1.10}$$

Here, e is the elementary charge, $\mathbf{j}$ is the current, a is the lattice constant, p is the spin polarization of the current and β is the magnitude of the force from the current due to non-adiabatic effects. The third and fourth terms are now due to an electronic current through the system, where the β-term does not come out from the derivation, instead it is added afterward as a way to include a force that is perpendicular to the force term coming from the current. One can imagine that it arises because the itinerant electrons are not perfectly aligned with the localized moments. The procedure gives an extra force in the LLG equation and the effect of the itinerant electrons is then reduced to a constant vector $\mathbf{j}$ in the equation of motion for the localized spins. This results in a linear dependence of the skyrmion velocity on the current [22–24]. However, if the system is simulated on a lattice, then there is a critical current j_c needed before the skyrmion starts to move [25]. A further simplification to skyrmion dynamics is given by the Thiele equation [22], which assumes that the skyrmion shape is constant. The Thiele equation is a drastic approximation, since only the center of mass (CM) of the skyrmion is simulated. It is given by

$$\mathbf{G} \times (\mathbf{v}_s - \mathbf{v}_d) + \mathbf{D}(\beta \mathbf{v}_s - \alpha \mathbf{v}_d) = 0, \tag{1.11}$$

$\mathbf{G} = (0, 0, 4\pi Q)$ is the gyromagnetic coupling vector, Q is the topological charge of the skyrmion which will be addressed in section 2.3, $\mathbf{D}$ is the dissipative force tensor, $\mathbf{v}_d$ is the velocity of the center of mass of the skyrmion and $\mathbf{v}_s = -\frac{pa^3}{2e}\mathbf{j}$ is the velocity of the itinerant electrons. The Thiele equation provides the following relationship for the current:

$$\mathbf{v}_d = \mathbf{v}_{\parallel} + \mathbf{v}_{\perp} \tag{1.12}$$

$$\mathbf{v}_{\parallel} = \left(\frac{\beta}{\alpha} + \frac{\alpha - \beta}{\alpha^3 (D/G)^2 + \alpha} \right) \mathbf{v}_s \qquad \mathbf{v}_{\perp} = \frac{(\alpha - \beta)(D/G)}{\alpha^2 (D/G)^2 + 1} (\hat{z} \times \mathbf{v}_s). \tag{1.13}$$

The Thiele equation is in good agreement with LLG equation simulations, except when the current is low or when the skyrmion disintegrates. The Thiele equation was originally proposed to model the steady state movement of magnetic domains [26]. Later it was adapted as a description of skyrmions, where it describes the center of mass motion of a skyrmion. It is a phenomenological equation, however, it can also be derived by an appropriate ansatz to the LLG equation [25]. The equation is simple enough that it allows for analytical solutions, which often capture effects observed in experiments such as the spin-Hall effect. However, as with the LLG equation, the Thiele equation is far from an ab initio calculation.

Clearly, an explicit inclusion of the electronic degrees of freedom should allow for a more detailed (microscopic) description of the skyrmion dynamics. To exemplify this point, let us look at a situation where we have a skyrmion in an otherwise ferromagnetic background coupled through a local Kondo coupling to itinerant electrons. The abrupt variation in the external magnetic field gives rise to interesting electrodynamics for the electrons passing by the skyrmion. There is an emergent electric field arising from the topological current density, and similarly there is an emergent magnetic field dependent on the topological charge density [25].

However, more interesting for our scopes is to view these interactions as torques. The itinerant electrons transfer their angular momentum to the localized spins when they flow through

the lattice, conversely the localized spins transfer their angular momentum to the localized spins. The phenomenon is called spin-transfer torque and a variation of it is used to create magnetic random-access memories [27]. Note that spin-transfer torque is only present if the spins involved in the process are not aligned, since otherwise the energy is already minimized in the Kondo-term.
Similarly, let us consider the case where the localized spins are in a state with a single skyrmion in an otherwise ferromagnetic background, and a spin-polarized bias is applied in the itinerant electrons such that spin-up electrons flow through the lattice. Thus, the itinerant electrons are spin-up when they reach the skyrmion. They will align with the localized moments of the skyrmion as they go through the skyrmion, assuming that the movement is adiabatic. In the center of the skyrmion the itinerant electrons will be spin down and when they are on the other side they return to spin up again. The twisting of the itinerant electrons passing over the skyrmion creates a force on the skyrmion, which could make it start to drift. In the Results chapter, we will see that at high enough currents the adiabatic picture is no longer valid.

2.3 Magnetic skyrmions

In the 1960:s, Tony Skyrme modeled nucleons with a non-linear sigma model [28], which describes scalar fields that have non-linear terms in the kinetic energy of the Lagrangian. Skyrme found that the conserved charge of the field was a winding number, which was interpreted as the baryon number [29]. To have baryons a non-trivial topology was needed, i.e. the field needed to twist N times to have N baryons. The topology stabilized the solution and thus the nucleons in Skyrme's model, now known as Skyrmions. Later skyrmions were also predicted in solid state systems [30, 31]. However, the experimental observation only came very recently [10, 32]. The advances in experimental technology and increased study of nano-scale systems has lead to a variety of different magnetic quasi-particles, some examples include magnetic vortices, bubbles and domain walls. Skyrmions are typically identified as a magnetic vortex with a non-zero integer topological charge. We consider two-dimensional systems from now on, but the discussion can be generalized to higher dimensions. As a function of where we are in the lattice (state space) the direction of the spin (target space) will change. In this context, the topology is in the mapping of the state space manifold D to the target space manifold S^2.

$$\mathcal{M} : D \to S^2 \tag{1.14}$$

The localized spins have a constant length and can point in any direction, hence the target space is a 2-sphere. If we impose either periodic boundary conditions or homogeneous boundary conditions:

$$\lim_{\mathbf{r}\to\mathbf{r}_\infty} \mathbf{n}(\mathbf{r}) = \mathbf{n}_0 \qquad \mathbf{n}(\mathbf{r}) = \mathbf{n}(\mathbf{r}+\mathbf{R}) \qquad \mathbf{r}_\infty, \mathbf{r}, \mathbf{R} \in \mathbb{R}^2, \tag{1.15}$$

then the state space can be compactified into $D = S^2$. Here, $\mathbf{n}$ is the normalized spin texture and $\mathbf{n}_0$ is the texture at the edge of the lattice. We can view the mapping $\mathcal{M}$ between the two 2-spheres as how a sphere can continuously wrap around another sphere. If the wrapping is continuous, it must wrap around integer times. The ways in which a continuous mapping

between a sphere of dimension i to a sphere of dimension n is known as the homotopy group of spheres $\pi_i(S^n)$ and to calculate such groups is in general a difficult task. Although when the dimension of the two spheres is the same, we always have that the group is the integers, i.e. in our case we have $\pi_2(S^2) = \mathbb{Z}$. For example, consider a state where all spins point upwards, that is described by zero wraps. Whereas if we have a single skyrmion, then we wrap around the sphere one time.

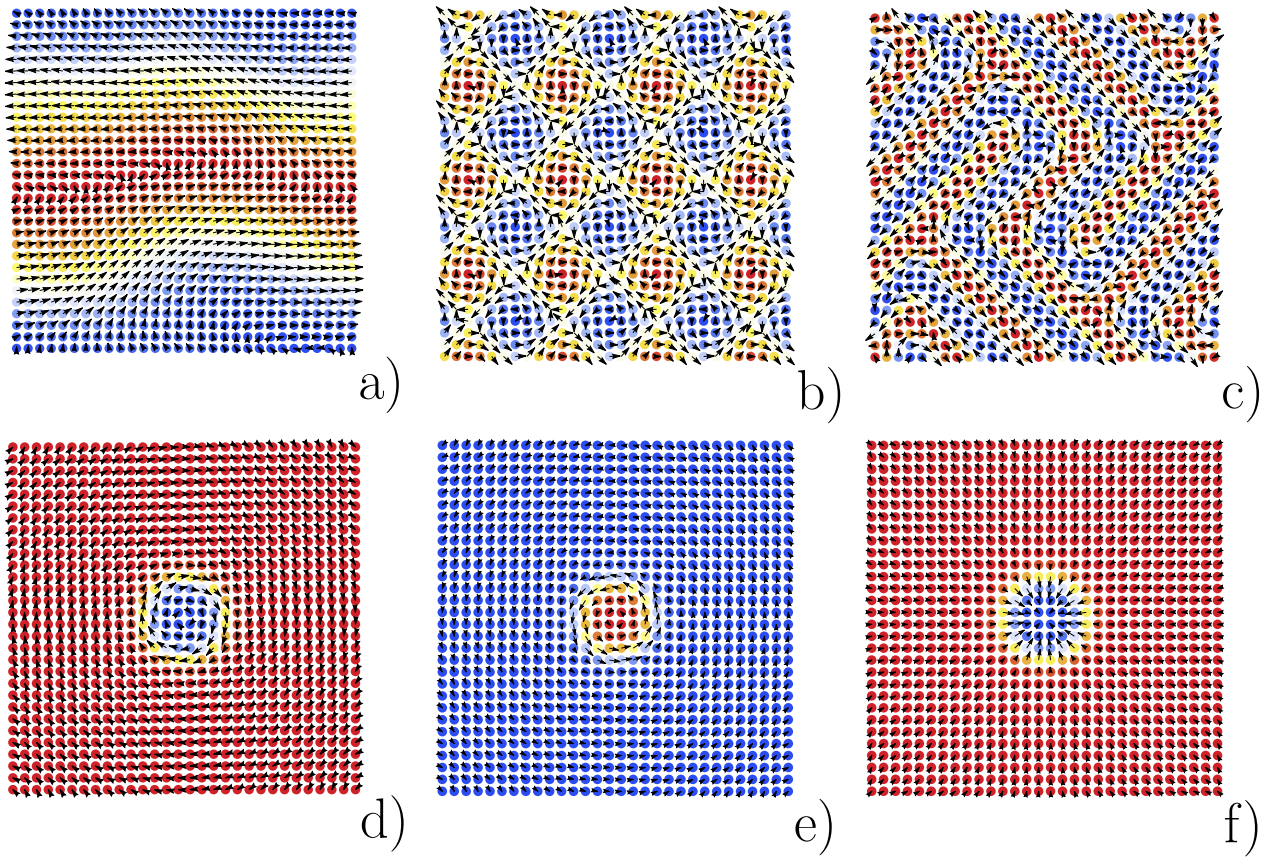

Figure 1.2: Some examples of spin-textures from the model in section 2.4. The DMI type is either Neel (N) or Bloch (B). The non-zero parameters are: a) $J = 0.5$ $D = 0.1$ (B), b) $J = 0.5$ $D = 0.1$ (B), c) $h = 0.05$ $J = 0.5$ $D = 0.8$ (B) $K = 0.6$, d) $h = 0.05$ $J = 0.5$ $D = 0.45$ (B) $K = 0.6$, e) $h = -0.05$, $J = 0.5$ $D = 0.45$ (B) $K = 0.6$ and f) $h = 0.05$ $J = 0.5$ $D = 0.45$ (N) $K = 0.6$. The color in the spins indicates the z-component, red is $+1$ and blue is -1, and the arrows indicate the direction in the xy-plane. The spin-textures have charges a) $Q = 0$, b) $Q = 0$, c) $Q = -2$, d) $Q = -1$, e) $Q = +1$ and f) $Q = -1$.

It is useful to consider a measure of how topology reflects into the system's physical properties. This generally corresponds to classify features which manifest as localized "defects" in a a topological sense. In the case of skyrmions, an suitable indicator is the topological charge, defined as:

$$Q = \frac{1}{4\pi} \int \mathrm{d}x\mathrm{d}y \, \overbrace{\mathbf{S} \cdot (\partial_x \mathbf{S} \times \partial_y \mathbf{S})}^{\equiv \rho(x,y)} = \frac{1}{4\pi} \int \mathrm{d}x\mathrm{d}y \, \rho(x, y). \tag{1.16}$$

Here, $\mathbf{S} = \mathbf{S}(x, y, t)$ is the spin density of the system, which is a function of the position and time. One can derive a continuity equation for the topological charge density [25],

$$\frac{\mathrm{d}}{\mathrm{d}t}\rho(x, y) + \boldsymbol{\nabla} \cdot \mathbf{j} = 0, \qquad \mathbf{j} = (\mathbf{S} \cdot \partial_y \mathbf{S} \times \dot{\mathbf{S}}, -\mathbf{S} \cdot \partial_x \mathbf{S} \times \dot{\mathbf{S}}, 0), \tag{1.17}$$

and if we are considering a large enough volume such that the current vanishes at the boundary of the volume, one can integrate this equation to find that the charge in (1.16) is conserved. In a continuum description, the topological charge is conserved. However, as soon as we go to a realistic system or a lattice model the topological charge is not guaranteed to be conserved. Skyrmions are stabilized by a finite energy barrier in the discrete case, once the skyrmion state has been created the system is stuck in a new local minima in the energy landscape. Typically it is the DMI that stabilizes skyrmions, but other ways are also possible [33].

In Fig. 1.2, we have some examples of spin textures. All textures except b) are fully relaxed. The spin texture in Fig. 1.2b), called a skyrmion crystal, is temporarily stable but relaxes to Fig. 1.2a) after some time. Skyrmion crystals have been observed in experiments [34], but with the parameters chosen the skyrmion crystal is not stable in our model. The topological charge of the spins in Fig. 1.2a) is zero, since we do not have a complete turn. Locally Fig. 1.2b) has topological charges, but for the whole lattice the charge is zero. The spin texture in Fig. 1.2c) has $Q = -2$, since there are two closed blue loops. However, this is not easy to see just by looking at the image. The last row of Fig. 1.2 displays typical skyrmion configurations.

The particular type of skyrmion that is realized in a system depends on the symmetry of the material. For example, in Fig. 1.2d), we have a Bloch skyrmion which looks like a vortex. Another common skyrmion type is a Neél skyrmion, shown in Fig 1.2f): in this case, the spins point outwards instead of along the boundary of the skyrmion. Skyrmions occur in very many materials and at different temperatures. For illustration, in Table 1 we give a few concrete examples of materials, together with the respective type of skyrmions supported. Often, but not always, Bloch skyrmions appear in bulk materials with broken inversion symmetry. Néel skyrmions are common for interfaces, where the surface breaks inversion symmetry.

Material	Skyrmion type	Temperature observed [K]	Wavelength λ_H
MnSi Thin Film	Bloch	<5-23	18 nm
FeGe Bulk	Bloch	273-278	70 nm
(Pt/Co/MgO) thin layer	Néel	$\gtrapprox$ 300	500 nm
$Ga\,V_4\,S_8$ Bulk	Néel	9-13	17.7 nm

Table 1.1: Some examples of materials where skymrions have been observed, taken from [12].

When moving to a lattice, it can be shown that a suitable definition of topological charge is [35]

$$Q = \frac{1}{4\pi} \sum_{\{i,j,k\}\in\Delta} \Omega_{ijk} \tag{1.18}$$

$$\exp(i\Omega_{ijk}/2) = (1 + \mathbf{S}_i \cdot \mathbf{S}_j + \mathbf{S}_j \cdot \mathbf{S}_k + \mathbf{S}_k \cdot \mathbf{S}_i + i\eta_{ijk}\mathbf{S}_i \cdot (\mathbf{S}_j \times \mathbf{S}_k))/\rho_{ijk} \tag{1.19}$$

$$\rho_{ijk} = \sqrt{2(1 + \mathbf{S}_i \cdot \mathbf{S}_j)(1 + \mathbf{S}_j \cdot \mathbf{S}_k)(1 + \mathbf{S}_k \cdot \mathbf{S}_i)} \tag{1.20}$$

The sum is over the triangulated lattice, where Δ is the set that contains the indices for the lattice sites which span the triangles for every triangle in the lattice. $\eta_{ijk} = \mathrm{sgn}(\mathbf{S}_i \cdot (\mathbf{S}_j \times \mathbf{S}_k))$, which ensures that the last term is positive. The formula for the topological charge is strictly speaking for classical spins, but the formula can be extended to quantum spins

$$\mathbf{S}_i = \frac{\langle \hat{\mathbf{S}}_i \rangle}{|\langle \hat{\mathbf{S}}_i \rangle|} \qquad\qquad Q = \frac{1}{4\pi} \sum_{\{i,j,k\}\in\Delta} \Omega_{ijk}(\mathbf{S}_i, \mathbf{S}_j, \mathbf{S}_k). \tag{1.21}$$

It is somewhat unsatisfactory that Q is not an observable in this formula. The scalar spin chirality is an alternative which is an observable

$$Q_{sc} = \frac{1}{\pi} \sum_{\{i,j,k\}\in\Delta} \hat{\mathbf{S}}_i \cdot \hat{\mathbf{S}}_j \times \hat{\mathbf{S}}_k, \tag{1.22}$$

but it is not an integer. This is the continuum definition of charge with $\mathbf{S}$ naively discretized as quantum spin operators, therefore it can give an indication whether or not we have a topological state but not more than that.

2.4 The effective Hamiltonian

Ideally one would want to do a full quantum mechanical calculation, where all microscopic details is taken into account, but this is far beyond the reach of computers today. An alternative is to do an ab initio DFT calculation with some approximation, such as the local density approximation for example, although it is not clear if that can capture the strongly correlated effects. Inspired by the success of the Kondo model, we will consider a system where there is a competition between itinerant and localized electrons. Therefore we will consider an effective Hamiltonian for s-d electron systems. The model presented could also describe a magnetic insulator or a thin film proximity coupled to a conductor, hence the 2D system could be realized on a thin film Fe/Ir(1,1,1) or Pd/Fe/Ir(1,1,1) proximity coupled to a conductor, hence the 2D system could be realized on a thin film Fe/Ir(1,1,1) or Pd/Fe/Ir(1,1,1) as further discussed in [2]. Here, (1,1,1) is the Miller index of the thin film. The system we consider is described by the following Hamiltonian:

$$H = H_s(t) + H_{s-d} + H_d, \tag{1.23}$$

where,

$$H_s(t) = \sum_{\langle ij \rangle} c^\dagger_{i\sigma}(-t_s \mathbb{I} + \boldsymbol{\alpha}_{ij} \cdot \boldsymbol{\tau})_{\sigma\sigma'} c_{j\sigma'} + \sum_{i\sigma} \epsilon_{i\sigma}(t)\hat{n}_{i\sigma} - \mathbf{B} \cdot \sum_i \hat{\mathbf{s}}_i, \tag{1.24}$$

$$H_{s-d} = -g \sum_i \hat{\mathbf{s}}_i \cdot \hat{\mathbf{S}}_i, \tag{1.25}$$

$$H_d = \sum_{\langle ij \rangle} \left[J_{ij}/2 \hat{\mathbf{S}}_i \cdot \hat{\mathbf{S}}_j + \mathbf{D}_{ij}/2 \cdot \hat{\mathbf{S}}_i \times \hat{\mathbf{S}}_j \right] - \mathbf{B} \cdot \sum_i \hat{\mathbf{S}}_i - K/2 \sum_i \hat{S}^2_{i,z}. \tag{1.26}$$

Here, and in the rest of the section, summation over repeated spin-indices is implicit. Also $c^\dagger_{i\sigma}$ ($c_{i\sigma}$) creates (annihilates) a itinerant electron on site i with spin σ, $d^\dagger_{i\sigma}$ ($d_{i\sigma}$) creates (annihilates) a localized electron on site i with spin σ, g is the Kondo coupling, $\mathbf{B}$ is an external magnetic field, J_{ij} is the Heisenberg exchange interaction which we will take to be on the form $J_{ij} = J$ unless otherwise stated and $\mathbf{D}_{ij}$ is the DMI. Henceforth, we will refer to the localized electrons as localized moments or localized spins. Furthermore, t_s is the ordinary hopping, $\boldsymbol{\alpha}_{ij}$ is the spin-orbit induced hopping, $\epsilon_{i\sigma}(t)$ is the on-site energy, $\hat{n}_{i\sigma} = c^\dagger_{i\sigma} c_{i\sigma}$, $\boldsymbol{\tau} = (\tau_x, \tau_y, \tau_z)^T$ is a vector containing the Pauli matrices, $\hat{\mathbf{S}}_i = d^\dagger_{i\sigma} \boldsymbol{\tau}_{\sigma\sigma'} d_{i\sigma'}$ and $\hat{\mathbf{s}}_i = c^\dagger_{i\sigma} \boldsymbol{\tau}_{\sigma\sigma'} c_{i\sigma'}$. Concerning the DMI we will only talk about the magnitude D and type, since the ij dependence is then clear:

$$\mathbf{D}_{ij} = D(j_x - i_x, j_y - i_y, 0)^T \text{ (Bloch)}, \qquad \mathbf{D}_{ij} = D(j_y - i_y, i_x - j_x, 0)^T \text{ (Néel)}. \tag{1.27}$$

Similarly for the Rashba spin-orbit coupling $\boldsymbol{\alpha}_{ij}$ we will only talk about the magnitude:

$$\boldsymbol{\alpha}_{ij} = i\alpha_R (j_y - i_y, i_x - j_x, 0)^T. \tag{1.28}$$

Note that the first i in this equation is the imaginary unit, whereas the second is the lattice site. One can imagine the directional dependence of $\boldsymbol{\alpha}_{ij}$ is gained due to the directional dependence of the angular momentum matrix elements in (1.3).

Clearly we have two systems that only interact via their spins, one system contains s-electrons and one contains d-electrons. In experiments, the skyrmions are observed in the localized d-electron spins. In Table 1.1, we can see that typically the wavelength of skyrmions is on the scale of tens of nanometers [12, 36], hence a classical treatment is often necessary. Considering a lattice spacing on the order of a few Ångström one realizes that there are roughly 100 spins across, therefore a two-dimensional skyrmion consist of $\sim$ 10000 spins. Such sizes are currently out of the reach of a full quantum treatment, and often they even justify a continuum limit, called the micromagnetic limit in the context of skyrmions.

Most people treat the localized spins classically through such micromagnetic simulations or more sophisticated atomistic models, where the lattice structure is considered. Nevertheless, these are entirely classical treatments, and in such simulations the s-electrons are neglected. Instead, in our approach we keep the s-electrons as they are and take the classical limit of the moments in (1.26) by letting $\hat{\mathbf{S}}_i \to \langle \hat{\mathbf{S}}_i \rangle$ and determining the time-evolution using the Ehrenfest theorem:

$$\frac{\mathrm{d}\mathbf{S}_i}{\mathrm{d}t} = \mathbf{S}_i \times \left[\sum_{\langle j \rangle} S(J_{ij}\mathbf{S}_j + \mathbf{D}_{ij} \times \mathbf{S}_j) - g\langle \hat{\mathbf{s}}_i \rangle - \hat{z}(B + KS_{i,z}) \right]. \tag{1.29}$$

The classical limit approximation is exact when $|\langle\hat{\mathbf{S}}_i\rangle| = S \to \infty$ [37, 38]. The result is an equation of the Landau-Lifshitz form, where we will add damping to get the full LLG equation as mentioned in section 2.2 except from the current. In our case, the current enters as the force $\mathrm{g}\langle\hat{\mathbf{s}}_i\rangle$. The spins have been rewritten as normalized vectors $\mathbf{S}_i = \langle\hat{\mathbf{S}}_i\rangle/S$. Since the localized spins are now classical, they act as a set of external fields on the itinerant spins.

2.5 Observables

We will calculate a few key observables in the coupled spin-electron system. First is the current from each spin-resolved lead α, where one can derive a formula by taking the derivative of the number of particles in each spin-resolved lead and multiplying the result with their charge: $I_\alpha = q\frac{\mathrm{d}\langle N_\alpha\rangle}{\mathrm{d}t}$. The particles in each lead can only go to the system. Hence the change of particles times their charge is current. If one assumes that the Matsubara components are included by attaching the leads slowly (we will discuss this in the next chapter section 1.5), then one gets the Meir-Wingreen formula for the current [39, 40]:

$$I_\alpha = 2q\mathrm{Re}\big\{\mathrm{Tr}(\left[\Sigma^<_\alpha \cdot G^A + \Sigma^R_\alpha \cdot G^<\right](t,t))\big\}. \tag{1.30}$$

In this form, it is clear that the current is essentially the trace of the collision integral. Hence there is no need for time-propagating this expression since one can take the trace of the collision integral. Another important quantity is the Density of states (DOS), given by:

$$D(E) = \sum_\lambda \delta(E - E_\lambda) \approx \sum_\lambda \frac{\epsilon/\pi}{(E-E_\lambda)^2 + \epsilon^2}. \tag{1.31}$$

, where E_λ is the eigenvalues of the Hamiltonian. Strictly speaking, the delta function is not a function, it is a distribution. However, when visualizing the density of states, one often replaces the delta functions with Lorentzians of finite width. In experiments, there is a broadening of the states due to either thermal effects or natural broadening. However, our ϵ is arbitrarily picked to aid the visualization of the DOS. The local density of states (LDOS), which we denote by $g(E,i,\sigma)$, is intimately related to the DOS:

$$g(E,i,\sigma) = \sum_\lambda \delta(E-E_\lambda)|\left\langle i\sigma|\lambda\right\rangle|^2, \qquad D(E) = \sum_{i\sigma} g(E,i,\sigma), \tag{1.32}$$

where i is the lattice site, σ is the spin and $|\lambda\rangle$ is the eigenstate. For the LDOS, one also needs to introduce a broadening in order to visualize. The form shows that the LDOS also gives local information; the delta functions are weighed such that the spectrum is dominated by the eigenstates, which are most prevalent on any given site and spin.
The Chern number is the hallmark of nontrivial topological behavior; for instance, it appears in the quantum Hall effect. In an adiabatic time-evolution, the system remains in its eigenstates $|n\rangle$ up to a phase.

$$|n(t)\rangle = e^{i\gamma_n(t)}e^{i\theta(t)}|n\rangle \tag{1.33}$$

Consider an adiabatic process where the parameters are $\{R_1,\ldots,R_N\}$ changed in a cyclic fashion. One can show that one of the phases, called the geometric phase, is given by [41]:

$$\gamma_n(C) = \oint_C \mathbf{A}_n \cdot \mathrm{d}\mathbf{R} = \int_A \underbrace{\boldsymbol{\nabla}\times\mathbf{A}_n}_{\mathbf{B}_n(R)} \cdot \mathrm{d}\mathbf{a}. \tag{1.34}$$

Under ordinary circumstances, $\gamma_n(C)$ is zero since the integral is over a closed loop C. However, one can not always find a single $\mathbf{A}_n(\mathbf{R})$ for all points R, where one of the conditions is that $\mathbf{B}_n$ is divergence-free. We will calculate the Chern number using the parameters $\{k_x, k_y\}$ using Berry's formula [42], although the formula can be used with any set of parameters.

$$\mathbf{B}_n(k_x, k_y) = \mathrm{Im} \sum_{m \neq n} \frac{\langle n(k_x, k_y) | \frac{\partial H(k_x, k_y)}{\partial k_x} | m(k_x, k_y) \rangle \ \langle m(k_x, k_y) | \frac{\partial H(k_x, k_y)}{\partial k_x} | n(k_x, k_y) \rangle}{(E_m(k_x, k_y) - E_n(k_x, k_y))^2} \tag{1.35}$$

The Chern number is now the integral over the Berry curvature:

$$C_n = \frac{1}{2\pi} \int_0^{2\pi} \int_0^{2\pi} B_n(k_x, k_y) \mathrm{d}k_x \mathrm{d}k_y. \tag{1.36}$$

The parameters k_x and k_y are the k-space points acquired when one Fourier transforms the Hamiltonian, which is justified by the fact that periodic boundary conditions are used when the Chern number is calculated.

CHAPTER 2

Methodology

1 Nonequilibrium Green's functions

1.1 The contour

We now turn to a discussion of how electrons are described within our scheme. In the absence of electron-electron (e-e) interactions, and for finite electron-spin systems, a wavefunction approach for the electrons is possible. However, with e-e interactions, and/or when the system is in contact with reservoirs, NEGF provide a natural formalism. In the following, we give those essential elements of the NEGF technique, necessary to follow the description of our approach, or more details the reader is referred to [43]. The time-evolution of the wavefunction is given by the time-evolution operator

$$\mathcal{U}(t,t_0)\,|\psi(t_0)\rangle = |\psi(t)\rangle \qquad\qquad i\frac{\mathrm{d}}{\mathrm{d}t}\mathcal{U}(t,t_0) = H(t)\mathcal{U}(t,t_0), \tag{2.1}$$

where $\hbar = 1$. The most general solution is given by:

$$\mathcal{U}(t,t_0) = \begin{cases} \mathcal{T}\left\{e^{-i\int_{t_0}^{t} H(t')\mathrm{d}t'}\right\} & t > t_0 \\ \bar{\mathcal{T}}\left\{e^{i\int_{t_0}^{t} H(t')\mathrm{d}t'}\right\} & t < t_0 \end{cases}, \tag{2.2}$$

where $\mathcal{T}$ is the time-ordering operator, which orders earlier times to the right. Similarly, we have defined an anti-chronological ordering operator $\bar{\mathcal{T}}$, which orders later times to the right. For example:

$$\mathcal{T}\{A(t)B(t+1)\} = B(t+1)A(t), \qquad \bar{\mathcal{T}}\{A(t)B(t+1)\} = A(t)B(t+1). \tag{2.3}$$

The expectation value of an operator is on the following form

$$O(t) = \langle\psi(t)|\,\hat{O}(t)\,|\psi(t)\rangle = \langle\psi(t_0)|\mathcal{U}(t_0,t)\hat{O}(t)\mathcal{U}(t,t_0)\,|\psi(t_0)\rangle \tag{2.4}$$

$$= \langle\psi(t_0)|\,\bar{\mathcal{T}}\Big\{e^{i\int_{t_0}^{t}H(t')\mathrm{d}t'}\Big\}\hat{O}(t)\mathcal{T}\Big\{e^{-i\int_{t_0}^{t}H(t')\mathrm{d}t'}\Big\}\,|\psi(t_0)\rangle \tag{2.5}$$

$$= \langle\psi(t_0)|\,\mathcal{T}_{\tilde{\gamma}}\Big\{e^{i\int_{t_0}^{t}H(t')\mathrm{d}t'}\hat{O}(t)e^{-i\int_{t_0}^{t}H(t')\mathrm{d}t'}\Big\}\,|\psi(t_0)\rangle \tag{2.6}$$

$$= \langle\psi(t_0)|\,\mathcal{T}_{\tilde{\gamma}}\Big\{\hat{O}(t)e^{-i\int_{\tilde{\gamma}}H(z')\mathrm{d}z'}\Big\}\,|\psi(t_0)\rangle\,, \tag{2.7}$$

we have ordered everything along the contour $\tilde{\gamma}$ (see fig. 2.1). In (2.5), the anti-chronological time-ordering operator orders everything along γ_- whereas the chronological time ordering operator orders everything along γ_+ and we have $O(t)$ in the middle. Clearly, this structure is captured by $\mathcal{T}_{\tilde{\gamma}}$. Even if $\hat{O}(t)$ is in the Schrödinger picture, we need to write out the time-dependence since we would not know where along the contour to put the operator $\hat{O}$

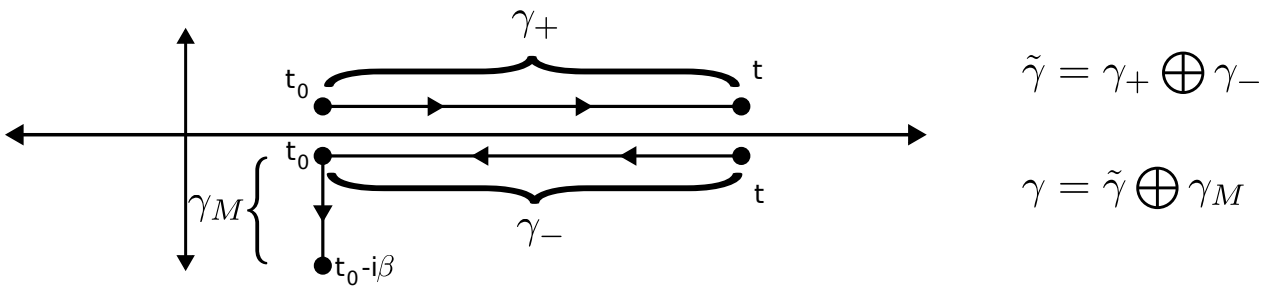

Figure 2.1: The contours drawn in the complex plane, γ_+ and γ_- are shifted an infinitesimal amount of the real axis. The end and start points of each contour are explicitly written. The arrows indicate the direction the operators are ordered.

The treatment above is useful if we are at zero temperature. If we consider finite temperature, i.e., a system prepared in a thermal bath, then we can extend the contour to include those effects. Consider a system with time-independent Hamiltonian H_M, which is prepared in a thermal bath at inverse temperature β. The ensemble average in quantum statistical physics is calculated by using the density matrix $\hat{\rho}$

$$O(z) = \mathrm{Tr}\Big(\hat{\rho}(z)\hat{O}(z)\Big) = \mathrm{Tr}\Big(\hat{\rho}\mathcal{T}_{\tilde{\gamma}}\Big\{\hat{O}(z)e^{-i\int_{\tilde{\gamma}}H(z')\mathrm{d}z'}\Big\}\Big) = \frac{\mathrm{Tr}\Big(e^{-H_M\beta}\mathcal{T}_{\tilde{\gamma}}\Big\{\hat{O}(z)e^{-i\int_{\tilde{\gamma}}H(z')\mathrm{d}z'}\Big\}\Big)}{\mathrm{Tr}(e^{-H_M\beta})} \tag{2.8}$$

$$= \frac{\mathrm{Tr}\Big(e^{-i\int_{\gamma_M}H_M\mathrm{d}z'}\mathcal{T}_{\tilde{\gamma}}\Big\{\hat{O}(z)e^{-i\int_{\tilde{\gamma}}H(z')\mathrm{d}z'}\Big\}\Big)}{\mathrm{Tr}\Big(e^{-i\int_{\gamma_M}H_M\mathrm{d}z'}\Big)}. \tag{2.9}$$

As long as the endpoints of the path γ_M satisfy

$$-i\beta = z_f - z_i, \tag{2.10}$$

we can have whatever path γ_M we want. The Hamiltonian is now defined along γ_M where we get H_M and along $\tilde{\gamma}$ we still get $H(t)$. Notice that:

$$\mathcal{T}_{\tilde{\gamma}}\Big\{e^{-i\int_{\tilde{\gamma}}H(z')\mathrm{d}z'}\Big\} = \mathcal{U}(t_0,t)\mathcal{U}(t,t_0) = \mathbb{I}. \tag{2.11}$$

Therefore we can write

$$\frac{\mathrm{Tr}\Big(e^{-i\int_{\gamma_M}H_M\mathrm{d}z'}\mathcal{T}_{\tilde{\gamma}}\Big\{\hat{O}(z)e^{-i\int_{\tilde{\gamma}}H(z')\mathrm{d}z'}\Big\}\Big)}{\mathrm{Tr}\Big(e^{-i\int_{\gamma_M}H_M\mathrm{d}z'}\Big)} = \frac{\mathrm{Tr}\Big(e^{-i\int_{\gamma_M}H_M\mathrm{d}z'}\mathcal{T}_{\tilde{\gamma}}\Big\{\hat{O}(z)e^{-i\int_{\tilde{\gamma}}H(z')\mathrm{d}z'}\Big\}\Big)}{\mathrm{Tr}\Big(\mathcal{T}_{\tilde{\gamma}}\Big\{e^{-i\int_{\tilde{\gamma}}H(z')\mathrm{d}z'}\Big\}e^{-i\int_{\gamma_M}H_M\mathrm{d}z'}\Big)} \tag{2.12}$$

$$= \frac{\mathrm{Tr}\Big(\mathcal{T}_{\gamma}\Big\{\hat{O}(z)e^{-i\int_{\gamma}H(z')\mathrm{d}z'}\Big\}\Big)}{\mathrm{Tr}\Big(\mathcal{T}_{\gamma}\Big\{e^{-i\int_{\gamma}H(z')\mathrm{d}z'}\Big\}\Big)}, \tag{2.13}$$

now the operators are ordered along the full γ in Fig. 2.1.

1.2 Kadanoff-Baym equations

We define the one-particle Green's function

$$G(1;2) = \frac{\mathrm{Tr}\Big(\mathcal{T}_{\gamma}\Big\{\hat{\psi}(1)\hat{\psi}^{\dagger}(2)e^{-i\int_{\gamma}H(z')\mathrm{d}z'}\Big\}\Big)}{i\,\mathrm{Tr}\Big(\mathcal{T}_{\gamma}\Big\{e^{-i\int_{\gamma}H(z')\mathrm{d}z'}\Big\}\Big)}, \tag{2.14}$$

Where, we have $j = 1, 2$ for points one and two in the correlation function. We will use the notation $j = (z_j, \mathbf{x}_j, \sigma_j)$ for brevity, we will later use the notation $j^{\pm} = (z_j \pm \eta, \mathbf{x}_j, \sigma_j)$ where η is an infinitesimal. The operator $\hat{O}(z)$ in the previous section has now been replaced with the field operators $\hat{\psi}(1)$ and $\hat{\psi}^{\dagger}(2)$, where the field operator $\hat{\psi}^{\dagger}(1)$ ($\hat{\psi}(1)$) creates (annihilates) a particle at position $\mathbf{x}_1$ with spin σ_1. Considering a general Hamiltonian for two-particle interactions

$$H(t) = \int \mathrm{d}\mathbf{x}\mathrm{d}\mathbf{x}'\hat{\psi}^{\dagger}(\mathbf{x})\hat{\psi}^{\dagger}(\mathbf{x}')v(\mathbf{x},\mathbf{x}')\hat{\psi}(\mathbf{x}')\hat{\psi}(\mathbf{x}) + \int \mathrm{d}\mathbf{x}\mathrm{d}\mathbf{x}'\hat{\psi}^{\dagger}(\mathbf{x})\,\langle\mathbf{x}|h(t)|\mathbf{x}'\rangle\,\hat{\psi}(\mathbf{x}'), \tag{2.15}$$

using the Heisenberg equation of motion on this Hamiltonian, one can show that the one-particle Green's function obeys the equation of motion.

$$i\frac{\mathrm{d}}{\mathrm{d}z_1}G(1;2) - \int \mathrm{d}3h(1;3)G(3;2) = \delta(1;2) - i\int \mathrm{d}3v(1;3)G_2(1,3;2,3^{+}) \tag{2.16}$$

$$-i\frac{\mathrm{d}}{\mathrm{d}z_2}G(1;2) - \int \mathrm{d}3G(1;3)h(3;2) = \delta(1;2) - i\int \mathrm{d}3G_2(1,3^{-};2,3)v(3;2), \tag{2.17}$$

where we have introduced the delta function along the contour and the two-particle GF:

$$G_2(1,2;\bar{1},\bar{2}) = \frac{\mathrm{Tr}\Big(\mathcal{T}_{\gamma}\Big\{\hat{\psi}(1)\hat{\psi}(2)\hat{\psi}^{\dagger}(\bar{2})\hat{\psi}^{\dagger}(\bar{1})e^{-i\int_{\gamma}H(z')\mathrm{d}z'}\Big\}\Big)}{i^2\,\mathrm{Tr}\Big(\mathcal{T}_{\gamma}\Big\{e^{-i\int_{\gamma}H(z')\mathrm{d}z'}\Big\}\Big)}. \tag{2.18}$$

The one-particle Hamiltonian and our potential are still time-diagonal

$$h(1;3) = \delta(t_1 - t_3)\,\langle \mathbf{x}_1|\hat{h}(t_1)|\mathbf{x}_3\rangle \qquad v(1;3) = \delta(t_1 - t_3)v(\mathbf{x}_1, \mathbf{x}_3), \tag{2.19}$$

G_2 can be written as:

$$-i\int \mathrm{d}3 v(1;3)G_2(1,3;2,3^+) = \int \Sigma(1;3)G(3;2) \tag{2.20}$$

$$-i\int \mathrm{d}3 G_2(1,3^-;2,3)v(3;2) = \int G(1;3)\Sigma(3;2). \tag{2.21}$$

We then get the Kadanoff-Baym equations [44]

$$i\frac{\mathrm{d}}{\mathrm{d}z_1}G(1;2) - \int \mathrm{d}3[h(1;3) + \Sigma(1;3)]G(3;2) = \delta(1;2) \tag{2.22}$$

$$-i\frac{\mathrm{d}}{\mathrm{d}z_2}G(1;2) - \int \mathrm{d}3 G(1;3)[h(3;2) + \Sigma(3;2)] = \delta(1;2), \tag{2.23}$$

we still have that h is time-diagonal but Σ is not guaranteed to be time-diagonal. Note that if we are working at the Hartree-Fock level, then Σ is time-diagonal. The integral kernel Σ is called the self-energy and it takes into account effects beyond the mean-field. We now make the integration with h over space implicit, i.e., in discrete form, it is a matrix multiplication.

$$\left[i\frac{\mathrm{d}}{\mathrm{d}z_1} - h(1)\right]G(1;2) = \delta(1;2) + \int \mathrm{d}3\Sigma(1;3)G(3;2) \tag{2.24}$$

$$G(1;2)\left[-i\frac{\overleftarrow{\mathrm{d}}}{\mathrm{d}z_2} - h(2)\right] = \delta(1;2) + \int \mathrm{d}3 G(1;3)\Sigma(3;2) \tag{2.25}$$

1.3 Langreth rules

We have introduced a framework to write the time dependence and equation of motion for an operator concisely. However, it is not clear how to solve these equations on the contour. Hence there is a need to project the equations onto the real axis. A function belongs to Keldysh space if it has the form

$$k(z,z') = k^\delta(z)\delta(z,z') + \theta(z,z')k^>(z,z') + \theta(z',z)k^<(z,z'), \tag{2.26}$$

and obeys

$$k^{\gtrless}(z_+,z') = k^{\gtrless}(z_-,z'), \qquad k^{\gtrless}(z,z'_+) = k^{\gtrless}(z,z'_-), \qquad k^\delta(z_+) = k^\delta(z_-) = k^\delta(z). \tag{2.27}$$

With $z_-, z'_- \in \gamma_-$ and $z_+, z'_+ \in \gamma_+$. The singular part k^δ is zero for the GF, but for the self-energy it represents the Hartree-Fock self-energy which is often absorbed into h. The $k^<$ is called the lesser component and $k^>$ is called the greater component. From now on, we consider only functions that belong to the Keldysh space. Notice that the field operators, and therefore all physical quantities of interest belong to Keldysh space. Now if we have a term on the form

$$c(t_1,t_2) = \int_\gamma \mathrm{d}z\, a(t_1,z)b(z,t_2), \tag{2.28}$$

we can always split the integration into several smaller intervals where $a(t_1, z)$ and $b(z, t_2)$ are written in terms of their Keldysh components $k^<$, $k^>$ and k^δ, which is the logic that underpins the Langreth rules. We will not derive the rules, but we present them below. First, we introduce a shorthand notation for integration over parts of the contour:

$$a \cdot b = \int_{t_0}^{t} \mathrm{d}z\, a(t_1, z) b(z, t_2) \qquad\qquad a * b = -i \int_0^\beta \mathrm{d}z\, a(t_1, z) b(z, t_2). \tag{2.29}$$

In the left-hand side, there is no explicit mention of the dependence on t_1 and t_2. However, this is understood from the context. If not, we will explicitly write out the dependence:

$$[a \cdot b](t_1, t_2). \tag{2.30}$$

Definition	$c(z,z') = \int_\gamma d\bar{z}\; a(z,\bar{z}) b(\bar{z},z')$	$c(z,z') = a(z,z')b(z',z)$ $[a^\delta = b^\delta = 0]$
$k^>(t,t') = k(t_+, t'_-)$	$c^> = a^> \cdot b^\mathrm{A} + a^\mathrm{R} \cdot b^> + a^\rceil \star b^\lceil$	$c^> = a^> b^<$
$k^<(t,t') = k(t_-, t'_+)$	$c^< = a^< \cdot b^\mathrm{A} + a^\mathrm{R} \cdot b^< + a^\rceil \star b^\lceil$	$c^< = a^< b^>$
$k^\mathrm{R}(t,t') = k^\delta(t)\delta(t-t') + \theta(t-t')[k^>(t,t') - k^<(t,t')]$	$c^\mathrm{R} = a^\mathrm{R} \cdot b^\mathrm{R}$	$c^\mathrm{R} = \begin{cases} a^\mathrm{R} b^< + a^< b^\mathrm{A} \\ a^\mathrm{R} b^> + a^> b^\mathrm{A} \end{cases}$
$k^\mathrm{A}(t,t') = k^\delta(t)\delta(t-t') - \theta(t'-t)[k^>(t,t') - k^<(t,t')]$	$c^\mathrm{A} = a^\mathrm{A} \cdot b^\mathrm{A}$	$c^\mathrm{A} = \begin{cases} a^\mathrm{A} b^< + a^< b^\mathrm{R} \\ a^\mathrm{A} b^> + a^> b^\mathrm{R} \end{cases}$
$k^\mathrm{T}(t,t') = k(t_-, t'_-)$	$c^\mathrm{T} = a^\mathrm{T} \cdot b^\mathrm{T} - a^< \cdot b^> + a^\rceil \star b^\lceil$	$c^\mathrm{T} = \begin{cases} a^< b^\mathrm{T} + a^\mathrm{R} b^< \\ a^\mathrm{T} b^> + a^> b^\mathrm{A} \end{cases}$
$k^{\bar{\mathrm{T}}}(t,t') = k(t_+, t'_+)$	$c^{\bar{\mathrm{T}}} = a^> \cdot b^< - a^{\bar{\mathrm{T}}} \cdot b^{\bar{\mathrm{T}}} + a^\rceil \star b^\lceil$	$c^{\bar{\mathrm{T}}} = \begin{cases} a^{\bar{\mathrm{T}}} b^< - a^< b^\mathrm{A} \\ a^> b^{\bar{\mathrm{T}}} - a^\mathrm{R} b^> \end{cases}$
$k^\rceil(t,\tau) = k(t_\pm, t_0 - i\tau)$	$c^\rceil = a^\mathrm{R} \cdot b^\rceil + a^\rceil \star b^\mathrm{M}$	$c^\rceil = a^\rceil b^\lceil$
$k^\lceil(\tau,t) = k(t_0 - i\tau, t_\pm)$	$c^\lceil = a^\lceil \cdot b^\mathrm{A} + a^\mathrm{M} \star b^\lceil$	$c^\lceil = a^\lceil b^\rceil$
$k^\mathrm{M}(\tau,\tau') = k(t_0 - i\tau, t_0 - i\tau')$	$c^\mathrm{M} = a^\mathrm{M} \star b^\mathrm{M}$	$c^\mathrm{M} = a^\mathrm{M} b^\mathrm{M}$

Figure 2.2: The Langreth rules, the table is taken from [43]. Here, t_+ means that it is along γ_+ and t_- means that it is along γ_-

The definition of the Keldysh components is given in the first column of the table. Along $\tilde{\gamma}$ (see Fig. 2.1) only $k^<$,$k^>$ and k^δ are needed in principle, but k^R, k^A, k^T and $k^{\bar{T}}$ are introduced to simplify equations. The retarded $k^R(t,t')$ and advanced $k^A(t,t')$ components have the useful feature that they vanish for $t < t'$ and $t > t'$ respectively. To be able to write functions of real variables along γ_M, we introduce the components k^M, $k^\rceil$, and $k^\lceil$. Here, k^M has both arguments along γ_M, while the tail of the symbols $\rceil$ and $\lceil$ indicate which of the two arguments are along γ_M.

The second column contains the rules to transfer our GFs and self-energies to functions of real variables, and that column will be the one that is primarily used in the derivations. In the last column, the table contains the information needed split a multiplication of two functions into its Keldysh components. In the following we will work with the the Keldysh components of the GF and of the self-energy.

1.4 Generalized Kadanoff-Baym ansatz

The Kadanoff-Baym ansatz was originally derived for a system in equilibrium and the limit of weak scattering; however, the ansatz is expected to be approximately valid in weak non-equilibrium. When the ansatz is transformed from the frequency domain into the time domain, it is not immediately clear if it obeys causality and certain asymptotic equations [45]. The solution was to slightly rearrange the terms within the ansatz such that these, among others, conditions were met. Due to the ad-hoc modification, there is no clear theoretical justification for the new ansatz, called the Generalized Kadanoff-Baym ansatz (GKBA). However, in practice, the ansatz is often accurate. When the ansatz was initially proposed, it was shown to correspond to a zeroth-order truncation of a Dyson-like equation. However, a zeroth order truncation is not expected to give good results. The ansatz is given by the following factorization [45]

$$G^<(t,t') = iG^R(t,t')G^<(t',t') - iG^<(t,t)G^A(t,t'). \tag{2.31}$$

GKBA has previously been studied in open system dynamics [46], where small 1D systems in contact with tight-binding leads were studied. The numerical results showed that GKBA is in good agreement with the full numerical solution in the limit of large hopping within the leads, called the wide-band limit (WBL).
In the context of magnetic systems, it has been pointed out that GKBA can fail severely when considering quantum transport [47]. The embedding self-energy is what makes electrons tunnel in and out of the system; hence the authors in [47] refer to it as a tunneling function. In that paper, a tunneling function with a rich *sd*-spectral structure was used, where the tunneling function had been obtained from a previous ab-into calculation. The result was that additional corrections beyond GKBA were needed. However, the WBL has a flat spectral dependence, and therefore, it is not clear if WBL+GKBA calculations will suffer from such problems.

1.5 Density matrix equation of motion

Using the Langreth rules on the Kadanoff-Baym equations (2.24) and (2.25), we can derive the following equation of motion for the lesser Green's function

$$\left[i\frac{\mathrm{d}}{\mathrm{d}t_1} - h(t_1)\right]G^<(t_1,t_2) = \delta(t_1-t_2) + \left[\Sigma^< \cdot G^A + \Sigma^< \cdot G^< + \Sigma^\rceil * G^\lceil\right](t_1,t_2) \tag{2.32}$$

$$G^<(t_1,t_2)\left[i\frac{\overleftarrow{\mathrm{d}}}{\mathrm{d}t_2} - h(t_2)\right] = \delta(t_1-t_2) + \left[G^< \cdot \Sigma^A + G^< \cdot \Sigma^< + G^\rceil * \Sigma^\lceil\right](t_1,t_2). \tag{2.33}$$

Now consider $\lim_{t_2\to t_1}$ ((2.32) + (2.33)) and relabel $t_1 \to t$.

$$i\frac{\mathrm{d}G^<(t,t)}{\mathrm{d}t} - [h(t), G^<(t,t)] = -\left[\Sigma^< \cdot G^A + \Sigma^R \cdot G^< + \Sigma^\rceil * G^\lceil\right](t,t) + h.c.$$

Assume initial correlations are washed out:

$$i\frac{\mathrm{d}G^<(t,t)}{\mathrm{d}t} - [h(t), G^<(t,t)] = -\left[\Sigma^< \cdot G^A + \Sigma^R \cdot G^<\right](t,t) + h.c.$$

Instead of including such Matsubara terms, we let the system equilibrate before we start the dynamics; hence we will have an unphysical regime at the beginning of the time evolution. The self-energy corresponds to the macroscopic leads in our case. Therefore, we will attach these slowly instead of having the Matsubara terms above. Such a procedure has been shown to be justified [48, 49]. We employ GKBA:

$$\begin{aligned} i\frac{\mathrm{d}G^<(t,t)}{\mathrm{d}t} - [h(t), G^<(t,t)] &= -\left[\int_{t_0}^{t} \mathrm{d}\bar{t}\, \Sigma^<(t,\bar{t})G^A(\bar{t},t) + \int_{t_0}^{t} \mathrm{d}\bar{t}\, \Sigma^R(t,\bar{t})G^<(\bar{t},t)\right] + h.c. \\ &= -\Bigg[\int_{t_0}^{t} \mathrm{d}\bar{t}\, \Sigma^<(t,\bar{t})G^A(\bar{t},t) + \int_{t_0}^{t} \mathrm{d}\bar{t}\, \Sigma^R(t,\bar{t})\Bigg(i\underbrace{G^R(\bar{t},t)}_{=0,\text{ since } t>\bar{t}} G^<(t,t) \\ &\quad - iG^<(\bar{t},\bar{t})G^A(\bar{t},t)\Bigg)\Bigg] + h.c. \\ &= -\left[\int_{t_0}^{t} \mathrm{d}\bar{t}\, \Sigma^<(t,\bar{t})G^A(\bar{t},t) + \int_{t_0}^{t} \mathrm{d}\bar{t}\, \Sigma^R(t,\bar{t})\rho(\bar{t})G^A(\bar{t},t)\right] + h.c. \end{aligned}$$

We used: $G^<(t,t) = -i\rho(t)$, and now write:

$$\frac{\mathrm{d}\rho(t)}{\mathrm{d}t} + i[h(t),\rho(t)] = -\left[\int_{t_0}^{t} \mathrm{d}\bar{t}\, \Sigma^<(t,\bar{t})G^A(\bar{t},t) + \int_{t_0}^{t} \mathrm{d}\bar{t}\, \Sigma^R(t,\bar{t})\rho(\bar{t})G^A(\bar{t},t)\right] + h.c. = R(t). \tag{2.34}$$

Which gives the time-evolution of the density matrix.

1.6 Wide band limit and non-interacting approximation

Consider a central system with leads $\alpha = 1, \ldots, M-1$ attached to it; these act as an environment that only interacts with the central system. The leads do not interact with each other. We write the leads in terms of their eigenstates $k\alpha$; the connection between system and environment eigenstates is a given by $T_{nk\alpha}$. The central system evolves with an arbitrary interacting Hamiltonian of our choice. Hence, we have the following structure

$$h_{\alpha\alpha} = \sum_k \epsilon_{k\alpha}(t) c^\dagger_{k\alpha} c_{k\alpha} \qquad h_{MM} = \sum_{mn} V_{mn}(t) c^\dagger_m c_n + \sum_{ijmn} v_{ijmn}(t) c^\dagger_i c^\dagger_j c_m c_n \tag{2.35}$$

$$h_{\alpha M} = \sum_{nk} \tilde{T}_{nk\alpha}(t) c^\dagger_n c_{k\alpha} + h.c. \qquad \tilde{T}_{nk\alpha}(t) = T_{nk\alpha}(t)s(t), \tag{2.36}$$

where the h_{MM} Hamiltonian corresponds to the Hamiltonian of our central system. As shown in the following, it is possible to integrate out the explicit dynamics of the leads, and exactly account for their contribution in terms of an additional self-energy in the propagator for the central regions. We will vary the hopping between system and environment using the function $s(t)$, where the hopping between leads and system is given by $t_l(t) = t_l s(t)$. The

Hamiltonian of system and environment can be written in block form.

$$H = \begin{pmatrix} h_{11} & 0 & \dots & h_{1M} \\ 0 & h_{22} & \dots & h_{2M} \\ \vdots & \vdots & \ddots & \vdots \\ h_{M1} & h_{M2} & \dots & h_{MM} \end{pmatrix}, \tag{2.37}$$

where every entry in the matrix is a block matrix. Consider writing the many-body self-energy in the same block form; since only h_{MM} contains interaction terms, we have $\Sigma_{\alpha\alpha'} = \delta_{\alpha M}\delta_{\alpha' M}\Sigma_{MM}$. On the other hand, the Green's function is not block-diagonal. Let us write the Kadanoff-Baym equations for the three types of Green's functions we have

$$\left[i\frac{\mathrm{d}}{\mathrm{d}z} - h_{\alpha\alpha}(z)\right] G_{\alpha\alpha}(z,z') = \delta(z,z') \tag{2.38}$$

$$\left[i\frac{\mathrm{d}}{\mathrm{d}z} - h_{\alpha\alpha}(z)\right] G_{\alpha M}(z,z') = h_{\alpha M}(z) G_{MM}(z,z') \tag{2.39}$$

$$\left[i\frac{\mathrm{d}}{\mathrm{d}z} - h_{MM}(z)\right] G_{MM}(z,z') = \delta(z,z') + \sum_{\alpha} h_{M\alpha} G_{\alpha M}(z,z') + \int_{\gamma} \Sigma_{MM}(z,\bar{z}) G_{MM}(\bar{z},z')\mathrm{d}\bar{z} \tag{2.40}$$

By direct substitution, one can verify that the Green's function for system-environment is given by

$$G_{\alpha M}(z,z') = \int_{\gamma} G_{\alpha\alpha}(z,\bar{z}) h_{\alpha M}(\bar{z}) G_{MM}(\bar{z},z')\mathrm{d}\bar{z}. \tag{2.41}$$

Therefore we get the following equation for the GF of the central system:

$$\begin{aligned} &\left[i\frac{\mathrm{d}}{\mathrm{d}z} - h_{MM}(z)\right] G_{MM}(z,z') = \delta(z,z') + \int_{\gamma} \sum_{\alpha} \underbrace{h_{M\alpha}(z) G_{\alpha\alpha}(z,\bar{z}) h_{\alpha M}(\bar{z})}_{\Sigma_{\alpha}(z,\bar{z})} G_{MM}(\bar{z},z')\mathrm{d}\bar{z} \\ &+ \int_{\gamma} \Sigma_{MM}(z,\bar{z}) G_{MM}(\bar{z},z')\mathrm{d}\bar{z} \\ &= \delta(z,z') + \int_{\gamma} [\Sigma_{MM}(z,\bar{z}) + \Sigma_{em}(z,\bar{z})] G(\bar{z},z'), \quad \text{where} \quad \Sigma_{em}(z,\bar{z}) = \sum_{\alpha} \Sigma_{\alpha}(z,\bar{z}). \end{aligned} \tag{2.42}$$

The only effect the environment has on the system is an extra contribution to the self-energy. Let us consider that the leads are described by a tight-binding Hamiltonian

$$h_{\alpha\alpha}(z) = -t_b \sum_{\langle ij \rangle} c_i^{\dagger} c_j + \sum_i V_{\alpha}(z) c_i^{\dagger} c_i. \tag{2.43}$$

For the tight-binding model, the eigenvalues and the eigenstates are known. Therefore, we can diagonalize $h_{\alpha\alpha}(z)$ and calculate the analytical form of Σ_{em}. In this case, the eigenstates are time-independent, which means $\tilde{T}_{nk\alpha}(t) = T_{nk\alpha}$. In order to adequately describe an

environment, the leads are semi-infinite. Meaning that the leads are infinitely long but only as wide as our system. Taking the wide-band limit (WBL) gives us the following formulas for the embedding self-energies [6, 46, 50]:

$$\Sigma^{<}_{em}(t,t') = i\sum_{\alpha}\Gamma_{\alpha}s(t)s(t')e^{-i\int_{t}^{t'}V_{\alpha}(\bar{t})\mathrm{d}\bar{t}}\int f(\epsilon-\mu)e^{-i\epsilon(t-t')}\mathrm{d}\epsilon \tag{2.44}$$

$$\Sigma^{R}_{em}(t,t') = -i\pi\delta(t-t')s(t)s(t)\sum_{\alpha}\Gamma_{\alpha} \tag{2.45}$$

The complete derivation is in Appendix 1. Physically the WBL means that the local density of states at the edge of the leads is taken to be constant, and practically the hopping t_b within the leads is taken to infinity while keeping the ratio $\gamma = t_l^2/t_b$ fixed. For the 1D tight-binding model, the local density of states at the first site is

$$D(\epsilon) = \frac{1}{2t_b}\sqrt{1-\left(\frac{\epsilon}{2t_b}\right)^2} \qquad \epsilon \in (-2t_b, 2t_b), \tag{2.46}$$

and as t_b becomes large, this semi-circle flattens out. However, in the direction perpendicular to the edge of the system, there is still variation in the density of states.

With all of these simplifications, the time-evolution is still quadratic in time since we need to propagate the integral in the RHS of eq. (2.34), i.e the collision integral. The difficult part is the advanced Green's function, which is written numerically in a discretized form: $G^A(j\Delta, t)$, where $j = 0, \ldots, N$. Hence, we need to update N advanced GFs to make a time step from $t = (N-1)\Delta$ to $t = N\Delta$. This means we need N^2 operations to get to time t. Hence it is quadratic in time.

In the G1-G2 scheme [5], one propagates the collision integral directly; this yields a time-linear scheme for most many-body self-energies [5]. To derive the evolution of the collision integral within the G1-G2 scheme, one takes the derivative of the collision integral, which gives you (among other things) the Hamiltonian of the system. With an embedding self-energy, it is not clear how to implement G1-G2 since the embedding self-energy is strictly speaking evolving with the Hamiltonian of the environment, and therefore, we get the Hamiltonian of the environment when taking the derivative.

Some authors have nevertheless continued along this route. As a result, an additional term, coming from the Green's function within Σ_{em}, needs to be time-evolved [51]. The scheme is time-linear. However, the new term is the same dimension as the environment, and therefore, the computational complexity scales with the dimension of the environment. Our environment is infinite, and therefore, this scheme is not applicable.

Another scheme was proposed in [6] where the integral in (2.44) is approximated by doing an efficient pole expansion of the Fermi function. Technically the Padé approximant of the Fermi-function is computed, which gives a sum of $1/\epsilon$-terms, and when performing the integral over ϵ in (2.44), we get a sum over the poles. The idea of the approximation was born around seven years earlier than the actual implementation, since people knew that the Padé approximant could be applied to calculate the current [52]. The current is mathematically very similar to the collision integral.

With this approximation, the time dependence of the embedding self-energy is changed. Now

when taking the derivative of the collision integral, one gets terms which have a simpler temporal dependence; hence the collision integral can be propagated directly, and the scheme is time-linear. The authors of this approach use a finite t_b, meaning that if one closes the contour using Jordan's lemma in (2.44), there are $\beta t_b/\pi$ poles within the contour. This could justify the procedure since one would need a maximum of $\beta t_b/\pi$ poles to find convergence; however, using an efficient pole expansion allows for much fewer poles. Nevertheless, at small t_b, it is not justified to use Jordan's lemma since the integral along the semi-circle might not vanish. The authors in [6] use 10-20 poles when applying their approach to a two-level system. Thus, 10-20 integrals must be computed for every α. All things considered, 40-80 quantities need to be updated at every time step, a significant improvement from quadratic time, albeit too costly for our needs (the system under consideration is fairly large).
In the treatment presented here, the reservoirs are semi-infinite and treated within the wide-band limit. Building on recent literature [6, 51], we consider a non-interacting approximation to the collision integral, which allows for high-speed computations with a linear time scaling. Our approach offers a good trade-off between computational time and accuracy and allows us to simulate finite but very large systems as required to describe skyrmions textures. We can solve the integral in (2.44) analytically

$$\Sigma^{<}_{em}(t,t') = \sum_\alpha \Gamma_\alpha s(t)s(t')e^{-i\int_t^{t'} V_\alpha(\bar{t})\mathrm{d}\bar{t}}\left(-e^{-i\mu(t-t')}\frac{\pi/\beta}{\sinh(\pi(t-t')/\beta)} - i\pi/2\delta(t-t')\right) \tag{2.47}$$

$$= \sum_\alpha \left(e^{-i\int_t^{t'} V_\alpha(\bar{t})\mathrm{d}\bar{t}}\Lambda_\alpha(t-t')s(t)s(t') - \Gamma_\alpha i\pi/2\delta(t-t')s^2(t)\right) \tag{2.48}$$

$$\Sigma^{R}_{em}(t,t') = -i\pi\delta(t-t')s^2(t)\sum_\alpha \Gamma_\alpha. \tag{2.49}$$

The derivation of (2.47) is in Appendix 1. It could be that there is a rewriting of $1/\sinh(t-x)$ into the form $f(t)g(x)$ that would yield an exact time-linear solution. However, we are not aware of such a rewriting. These analytical forms are nevertheless useful since one can now consider approximations to the sinh function instead of the whole lesser self-energy. The dependence on t and t' in the lesser self-energy is not as clear. Instead of approximating the self-energy, we will consider another route; rather, we approximate the advanced Green's function directly. Another way to make the RHS of (2.34) time-linear is to write everything on the form $f(t-x)$. Hence we make the following approximation

$$\int_{t_0}^{t}\mathrm{d}\bar{t}\sum_\alpha e^{-i\int_t^{\bar{t}} V_\alpha(\tilde{t})\mathrm{d}\tilde{t}}\Lambda_\alpha(t-\bar{t})s(t)s(\bar{t})G^A(\bar{t},t') \approx \int_{t_0}^{t}\mathrm{d}\bar{t}\sum_\alpha e^{-i\int_t^{\bar{t}} V_\alpha(\tilde{t})\mathrm{d}\tilde{t}}\Lambda_\alpha(t-\bar{t})s(t)s(\bar{t})G^0(t-\bar{t})$$

$$G^A(t,t') = i\theta(t'-t)e^{i\int_t^{t'}\mathrm{d}x\,(H_0+H_S(x))} \approx G^0(t-t') \qquad G^0(t-t') = i\theta(t'-t)e^{i\int_t^{t'}\mathrm{d}x\,H_0}, \tag{2.50}$$

where $H_S(x)$ is the Kondo interaction between the localized spins and itinerant electrons. This is a drastic approximation; however, it is also a very practically useful simplification and corresponds to neglecting a higher-order effect. The spins are not coupled explicitly to the leads; the spins only interact with the electrons. The spin Hamiltonian in the advanced Green's function describes a process where the leads interact with the electrons, which in turn interact with the spins. Within our approximation, this process can still happen, but

then it happens in two steps. We attach the system and leads during a time τ and apply the bias suddenly after the leads have been attached

$$s(x) = \begin{cases} \sin^2(\pi x/2\tau) & \text{if } x < \tau \\ 1 & \text{else} \end{cases} \qquad V_\alpha(x) = \theta(x-\tau) \begin{cases} V & \text{if } \alpha = L\uparrow \\ -V & \text{if } \alpha = R\uparrow . \\ 0 & \text{otherwise} \end{cases} \tag{2.51}$$

With these reasonable choices, the term under integration in (2.50) can be written on the form $\sum_i A_i(t-\bar{t})$; thus, the time-evolution can be made time-linear. The details are given in Appendix 2. With this procedure, one quantity needs to be time-propagated every time-step when $t \leq \tau$, and two when $\tau < t$. We will consider the low-temperature limit, but the approach is the same for finite temperatures. For future reference, we call the approximation, approximated wide band limit (AWBL)

2 Numerical Implementation

2.1 Propagation of electrons

To solve (2.34) we do the following ansatz:

$$\rho(t) = U(t,0)r(t)U^\dagger(t,0) \qquad\qquad U(t,0) = \mathcal{T}\left\{e^{-i\int_0^t h(x)\mathrm{d}x}\right\} \tag{2.1}$$

This gives an equation for $r(t)$

$$\frac{\mathrm{d}r(t)}{\mathrm{d}t} = U^\dagger(t,0)R(t)U(t,0). \tag{2.2}$$

We can integrate this equation

$$r(T+\Delta) - r(T) = \int_T^{T+\Delta} U^\dagger(t,0)R(t)U(t,0)\mathrm{d}t \tag{2.3}$$

$$= \int_0^{\Delta} U(0,T+u)R(T+u)U(T+u,0)\mathrm{d}u \tag{2.4}$$

$$= U(0,T)\underbrace{\int_0^{\Delta} U(T,T+u)R(T+u)U(T+u,T)\mathrm{d}u}_{I}\,U(T,0). \tag{2.5}$$

Now we approximate the Hamiltonian in the propagator and $R(T+u) \approx R = (R(T+\Delta) + R(T))/2$ with their midpoint values

$$U(T+u,T) \approx e^{-ih(u+\mathcal{O}(u^3))} \qquad\qquad h = (h(T)+h(T+\Delta))/2. \tag{2.6}$$

Using the Campbell-Baker-Hausdorff formula

$$I = \int_0^{\Delta}\left(R + i(u+\mathcal{O}(u^3))[h,R] - \frac{(u+\mathcal{O}(u^3))^2}{2!}[h,[h,R]] - \frac{i(u+\mathcal{O}(u^3))^3}{3!}[h,[h,[h,R]]] + \ldots\right)\mathrm{d}u$$
$$= \Delta R + i\frac{\Delta^2+\mathcal{O}(\Delta^4)}{2}[h,R] - \frac{\Delta^3+\mathcal{O}(\Delta^5)}{3!}[h,[h,R]] - \ldots \tag{2.7}$$

$$\rho(T+\Delta) = U(T+\Delta,0)r(T+\Delta)U^\dagger(T+\Delta,0) \tag{2.8}$$

$$= U(T+\Delta,T)[\rho(T)+I]U^\dagger(T+\Delta,T). \tag{2.9}$$

The number of commutators to include in (2.7) is a convergence parameter just like the time-step. There is a local error $\mathcal{O}(\Delta^3)$ coming from the term $R\Delta$, since that term can be derived using the midpoint formula of the integral. Therefore one does not gain much by going to higher orders than two, nevertheless a local error of $\mathcal{O}(\Delta^3)$ is good enough for our purposes. In eq. (2.9) we can see that the I is what creates non-unitary dynamics, it can be traced back to the ansatz, which required $r(t)$ instead of $\rho(0)$ as in unitary dynamics. The value of the Hamiltonian $h(T+\Delta)$ and the RHS $R(T+\Delta)$ is not known at time T, therefore a predictor-corrector method will be used.

2.2 Propagation of spins

One could naively propagate the Landau-Lifshitz equation:

$$\frac{\mathrm{d}\mathbf{S}_i}{\mathrm{d}t} = \mathbf{F}_i(t) \times \mathbf{S}_i(t) = \mathbf{A}_i(t, \mathbf{S}_i), \tag{2.10}$$

using a normal differential equation solver such ha fourth-order Runge-Kutta:

$$\mathbf{S}_i(t+\Delta) = \mathbf{S}_i(t) + \frac{\Delta}{6}([\mathbf{A}_i]_1 + 2[\mathbf{A}_i]_2 + 2[\mathbf{A}_i]_3 + [\mathbf{A}_i]_4), \tag{2.11}$$

where $[\mathbf{A}_i]_1$, $[\mathbf{A}_i]_2$, $[\mathbf{A}_i]_3$ and $[\mathbf{A}_i]_4$ is the right hand side of (2.10) evaluated for various times and spins. Now take the square magnitude of both sides in (2.11):

$$|\mathbf{S}_i(t+\Delta)|^2 = |\mathbf{S}_i(t)|^2 + \left|\frac{\Delta}{6}([\mathbf{A}_i]_1 + 2[\mathbf{A}_i]_2 + 2[\mathbf{A}_i]_3 + [\mathbf{A}_i]_4\right|^2. \tag{2.12}$$

The cross terms are approximately zero since $\mathbf{F}_i(t) \times \mathbf{S}_i(t) \cdot \mathbf{S}_i(t) = 0$. We can see that the norm of the spins is not constant unless $\mathbf{A}_i = 0$. The drifting of the norm will happen with any numerical solver of the form (2.11). Instead we consider a geometric integrator, called the Depondt-Mertens algorithm [53], which does not change the norm. Since the spins evolve on the unit sphere, the solution is a SO(3) rotation matrix:

$$\mathbf{S}_i(t) = Q_i(t)\mathbf{S}_i(0). \tag{2.13}$$

To obtain the matrix $Q(t)$ is a difficult task, instead we consider:

$$Q_i(t+\Delta) \approx R_i(t^*)Q_i(t), \qquad t^* \in [t, t+\Delta]. \tag{2.14}$$

Where R is a rotation matrix, hence we can update the spins explicitly

$$\mathbf{S}_i(t+\Delta) = R_i(t^*)\mathbf{S}_i(t), \qquad t^* \in [t, t+\Delta].$$

Now if we take the magnitude of both sides we can see that norm is conserved due to $R^T R = \mathcal{I}$. The matrix form of the rotation is given by:

$$R_i = \begin{pmatrix} h_x^2 u + \cos\omega & h_x h_y u - h_z \sin\omega & h_x h_z u + h_y \sin\omega \\ h_x h_y u + h_z \sin\omega & h_y^2 u + \cos\omega & h_z h_y u - h_x \sin\omega \\ h_x h_z u - h_y \sin\omega & h_y h_z u + h_x \sin\omega & h_z^2 u + \cos\omega \end{pmatrix}. \tag{2.15}$$

The site index i has been dropped in the matrix for brevity, all of these quantities have time and spin dependence which is not explicitly written. The rotation axis is $\mathbf{h}_i = \mathbf{F}_i/|\mathbf{F}_i|$, the rotation angle is $\omega = \Delta|\mathbf{F}_i|$ and $u = 1 - \cos\omega$.

2.3 Code

The code was written in FORTRAN. To find the initial configuration of the spins, we do a simulated annealing procedure, where the temperature is slowly decreased in a Monte-Carlo simulation of the spins. This gives us an initial configuration which is loaded in before performing a simulation.

We introduce the itinerant electrons by finding the self-consistent initial state with the spins. This is done by introducing a Gilbert-damping in the spin equation of motion and doing the following loop a set number of times:

1. Calculate forces on the spins from the other spins $\mathbf{F}_{i,S}$, the forces from the electrons on the spins $\mathbf{F}_{i,el}$ using $|\Phi\rangle$ and $\mathbf{S}_i$. If this is the first iteration put $\mathbf{F}_{i,el} = 0$.
2. Find the Hartree-Fock ground state $|\Phi^p\rangle$ by diagonalizing the Hamiltonian $h(\mathbf{S}_i)$.
3. Propagate the spins one time-step $\mathbf{S}_i \to \mathbf{S}_i^p$, using the forces $\mathbf{F}_{i,el}$ and $\mathbf{F}_{i,S}$.
4. Find predicted forces $\mathbf{F}_{i,el}^p$ and $\mathbf{F}_{i,S}^p$ from $|\Phi^p\rangle$ and $\mathbf{S}_i^p$ respectively.
5. Find the new HF ground state $|\Phi\rangle$ by diagonalizing $h((\mathbf{S}_i + \mathbf{S}_i^p)/2)$
6. Propagate the spins one time-step $\mathbf{S}_i \to \mathbf{S}_i$, using the forces $(\mathbf{F}_{i,el} + \mathbf{F}_{i,el}^p)/2$ and $(\mathbf{F}_{i,S} + \mathbf{F}_{i,S})/2$ and go to 1

However, before this iteration starts the spins are relaxed in absence of electrons, since this is computationally much easier and therefore makes convergence faster.
After the initial state has been found the coupled system time-evolves by a predictor-corrector method similiar to the on used to find the initial state

1. Calculate forces on the spins from the other spins $\mathbf{F}_{i,S}(t)$, the forces from the electrons on the spins $\mathbf{F}_{i,el}(t)$ using $\rho(t)$ and $\mathbf{S}_i(t)$.
2. Propagate $R(t) \to R^p(t + dt)$
3. Propagate $\rho(t) \to \rho^p(t + dt)$ with (2.34) using $(R(t) + R^p(t + dt))/2$ and $h(\mathbf{S}_i(t))$
4. Propagate $\mathbf{S}_i(t) \to \mathbf{S}_i^p(t + dt)$, using the forces $\mathbf{F}_{i,el}(t)$ and $\mathbf{F}_{i,S}(t)$.
5. Find predicted forces $\mathbf{F}_{i,el}^p(t + dt)$ and $\mathbf{F}_{i,S}^p(t + dt)$ from $\rho^p(t + dt)$ and $\mathbf{S}_i^p(t + dt)$ respectively.
6. Propagate $R(t) \to R(t + dt)$ using $\rho^p(t + dt)$
7. Propagate $\rho(t) \to \rho(t + dt)$ using $(R(t) + R(t + dt))/2$ and $h((\mathbf{S}_i(t) + \mathbf{S}_i^p(t + dt))/2)$
8. Propagate $\mathbf{S}_i(t) \to \mathbf{S}_i^p(t + dt)$, using the forces $(\mathbf{F}_{i,el}(t) + \mathbf{F}_{i,el}^p(t + dt))/2$ and $(\mathbf{F}_{i,S}(t) + \mathbf{F}_{i,S}(t + dt)^p)/2$.
9. set $t \to t + dt$ and go to 1

CHAPTER 3

Results

1 Skyrmion transport

In this chapter, we present results for the skyrmion dynamics in the presence of leads when a symmetric spin-up bias is applied. In our experience, a spin-polarized bias must be used to move skyrmions with currents consistently. The Thiele and LLG equations support this since the current has zero effect when $p = 0$ in (1.13) and (1.10) respectively. The leads are connected to the spins+electrons central region according to a slow switching-on protocol, while the bias is applied suddenly. Their explicit temporal profile is shown in (2.51). As previously discussed, in the literature skyrmion transport is almost always dealt with using the LLG or the Thiele equation, yielding a linear velocity as a current function. As a first case study, we consider the movement of the center of mass (CM) of the skyrmion when various biases are applied.
We will use the same set of parameters in this section unless otherwise stated. We use: $g = 1$, $\mathbf{B} = (0, 0, 0.05)$, $t_s = -1$, $K = 0.6$, $\alpha = 0.01$, $\alpha_R = 0$, $J = 0.5$, $D = 0.4$ (Bloch type), $\gamma = 0.1$, $\tau = 200$, $\mu = 0$ (start at half-filling) and $V = 2$. In order to make the skyrmion stable in the benchmark, we had to use different parameters due to the small size of the system. When considering the skyrmion velocity as a function of current and bias, we need to vary the bias and increase the coupling between leads and system to get access to the non-linear regime of velocity as a function of current.

1.1 Approximation benchmark

To benchmark the approximated wide band limit (AWBL), we consider a small system that still captures the relevant physics. We use a 16-site strip which is two sites wide and attach the leads during 200 units of time, whereafter a symmetric spin-up bias is applied. To benchmark skyrmion transport, we start with the skyrmionic initial state; however, in a strict sense, the configuration would not be considered a skyrmion. After the bias has been applied for 300 units of time, we look qualitatively at how much the skyrmion has moved in both cases.

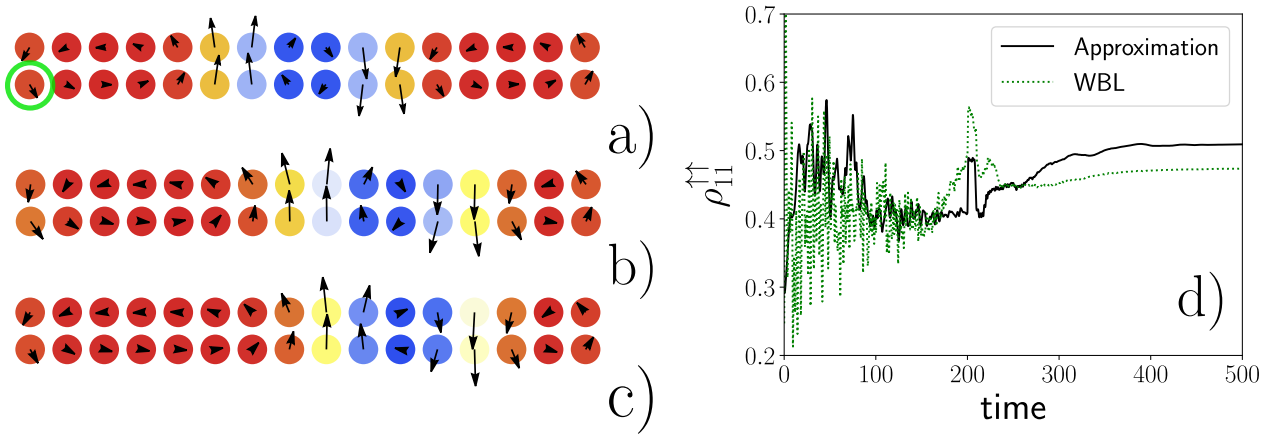

Figure 3.1: Benchmarking the AWBL treatment of the leads using a 2x16 spin texture and a corresponding layer of electrons. a) the initial relaxed spin structure; b) the spin texture at t=500 obtained via the exact WBL, c) the same structure at t=500 as obtained from the approximate treatment and d) shows the spin-up occupation of the first site, which is circled in green in a). $g = 1$, $\mathbf{B} = (0, 0, 0.05)$, $t_s = -1$, $K = 0.6$, $\alpha = 1$, $\alpha_R = 0$, $J = 0.5$, $D = 0.4$ (Bloch type), $\gamma = 0.5$, $\tau = 200$, $\mu = 0$ (start at half-filling) and $V = 3$. The color in the spins indicates the z-component red is $+1$ and blue is -1, and the arrows indicate the direction in the xy-plane

There is a disagreement in the occupation when the leads are attached, from t=0 to t=200 (see Fig. 3.1d)). Once the leads have been attached and the bias has been applied, the behavior remains qualitatively the same. However, we note that this regime is of no physical relevance here, and only needed to connect adiabatically system and leads.
Likewise, the movement of the spin texture is in the same direction in both cases. It is expected that the current is slightly different in the full WBL compared to AWBL since, in the AWBL, a factor in the collision integral is neglected.

1.2 Base case

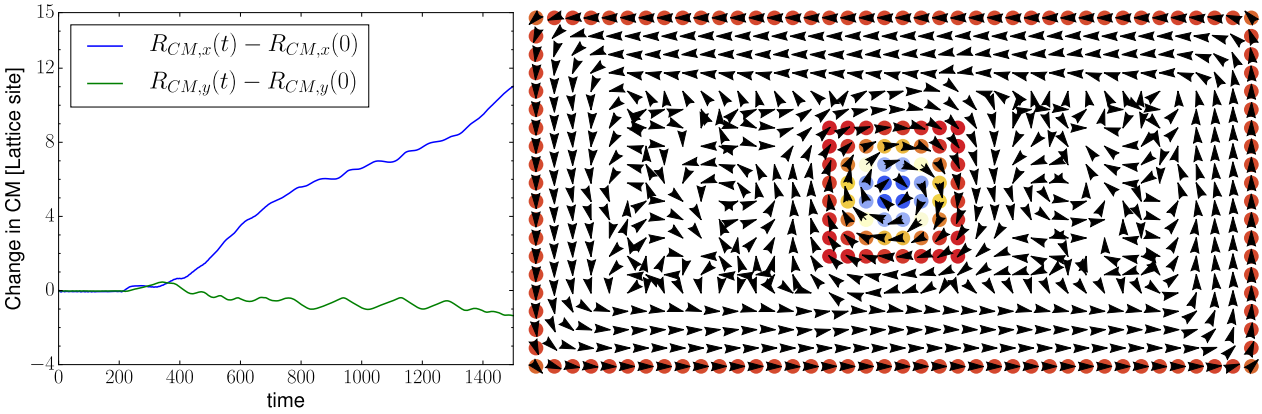

Figure 3.2: (left) the movement of the center of mass and (right) the spins at t=200. To highlight the non-trivial topology, the z-component is removed from the spins in the ferromagnetic sea since they are just spin-ups. $g = 1$, $\mathbf{B} = (0, 0, 0.05)$, $t_s = -1$, $K = 0.6$, $\alpha = 0.01$, $\alpha_R = 0$, $J = 0.5$, $D = 0.4$ (Bloch type), $\gamma = 0.1$, $\tau = 200$, $\mu = 0$ (start at half-filling) and $V = 2$. The color in the spins indicates the z-component red is $+1$ and blue is -1, and the arrows indicate the direction in the xy-plane.

In this section, we analyze the role of disorder (i.e. the presence of impurities) on skyrmion dynamics. To have reference results, we consider a region of 40x20 spins, and look at the dynamics of a clean sample (henceforth referred to as "base case"). In the base case and in the impurity cases, we have a potential $V = 2$ in the leads and coupling $\gamma = 0.1$ between system and leads. The skyrmion starts off with the relaxed spin texture in the center and starts to drift towards the right corner, with a slight movement downwards. There is a force right due to the current, but the force downwards must be due to something else. Namely, it is due to the spin-hall effect, which in this context can be thought of as the Magnus force in fluid dynamics. When a sphere moves in a straight line through a fluid while rotating, the Magnus force causes the trajectory to bend away from the expected straight path.
We can see that the velocity in the x-direction is not linear. The velocity ramps up, then slows down, and finally starts to ramp up again. Additionally, there are some small-scale oscillations, which are especially visible in the y-direction. The oscillations could be due to the discrete nature of the lattice sites since the skyrmion has an ideal radius at which it occurs. When it is between lattice sites, the skyrmion gets distorted but returns to the original configuration when it is at the new site. The skyrmion moves very slowly, in the y direction. Overall, the results is that the skyrmion oscillates back and forth a few times before going to a new site.

1.3 Impurity cases

We know the trajectory the skyrmion takes in the base case. Hence we can put impurities in its path. In the heatmaps of Figs. 3.3-3.5, the impurities are marked in green, where the impurities correspond to a reduction in the symmetric exchange interaction J. The

symmetric and antisymmetric exchange interactions are how the spins interact. Therefore, it is expected that the skyrmion will be hindered by a smaller interaction. Technically we reduce the coupling on a few sites as follows:

$$J_{ij} \to J/2, \tag{3.1}$$

which is changed at $t = 100$ to not disturb the system before the bias is applied at $t = 200$.

Case 1: A small impurity on the skyrmion path

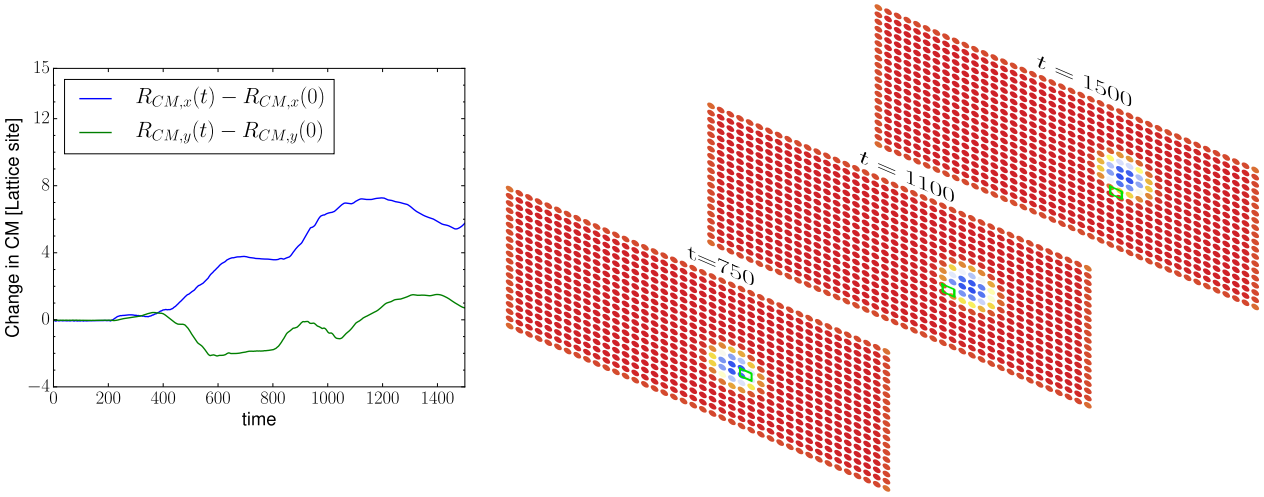

Figure 3.3: The center of mass movement of the skyrmion (left), and some snapshots of the z-component of the localized spins (right). $g = 1$, $\mathbf{B} = (0, 0, 0.05)$, $t_s = -1$, $K = 0.6$, $\alpha = 0.01$, $\alpha_R = 0$, $J = 0.5$, $D = 0.4$ (Bloch type), $\gamma = 0.1$, $\tau = 200$, $\mu = 0$ (start at half-filling) and $V = 2$. The color in the spins indicates the z-component red is $+1$ and blue is -1, and the arrows indicate the direction in the xy-plane.

As an example of small impurity disturbance, we consider a square of four lattice sites where the exchange is reduced. One can imagine that such disorder is due to an adsorbate atom in the center of these four lattice sites. These lattice sites are right in the path of the skyrmion, i.e., to the right of the skyrmion's initial position, and shifted one lattice site downwards since the skyrmion travels slightly downwards in the base case.
Looking at the movement of the center of mass in Fig. 3.3. In the x-direction, it seems like the skyrmion does not feel the effect of the impurity until it is on top of it, since the movement of the center of mass is quite similar to the base case before $t \sim 750$. However, if one looks closely, it moves slightly slower. The y-movement tells a different story; rather, in the y-direction, the skyrmion starts to pick up speed when it approaches the impurity. One could imagine that it is the movement in the x-direction which is transferred downwards.
After the skyrmion has entered the impurity, it can not escape; from $t = 750$ to $t = 1500$, the skyrmion is stuck to the impurity. The skyrmion can move around as long as some part is still on the impurity, which is what we see after $t = 750$. A few times during the dynamics, there are bumps, which indicate that the skyrmion gathered velocity to try to escape but was pulled back again by the impurity.

Case 2: A small impurity near the skyrmion path

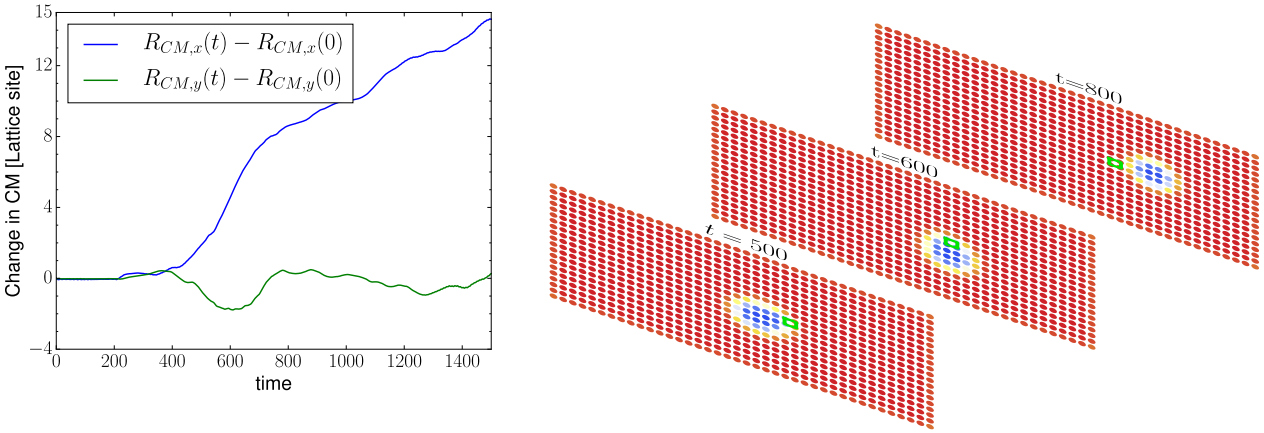

Figure 3.4: The center of mass movement of the skyrmion (left), and some snapshots of the z-component of the localized spins (right). $g = 1$, $\mathbf{B} = (0, 0, 0.05)$, $t_s = -1$, $K = 0.6$, $\alpha = 0.01$, $\alpha_R = 0$, $J = 0.5$, $D = 0.4$ (Bloch type), $\gamma = 0.1$, $\tau = 200$, $\mu = 0$ (start at half-filling) and $V = 2$. The color in the spins indicates the z-component red is $+1$ and blue is -1, and the arrows indicate the direction in the xy-plane.

Looking at Fig. 3.4, one can see that the impurity is moved two lattice sites upwards compared to the previous case; now, the impurity is slightly below the skyrmion's path. At the beginning of the dynamics, the movement seems very similar to the previous case, i.e., the x-movement is slightly reduced, and there is a significant movement downwards.
Nevertheless, the movement does not force the skyrmion inside the impurity. In the center of the mass movement of Fig. 3.4, and the snapshots at $t = 500$, $t = 600$ and $t = 800$ of Fig. 3.4, one can see that the skyrmion goes underneath the impurity. If the system is infinite, then the skyrmion would continue downwards. This illustrates at the microscopic level, an important constraint in racetrack memory engineering: namely, one wants a racetrack that is large enough such that the skyrmions can get around but not so large that the skyrmion can escape.
From the movement which is seen we speculate that there is a repulsive force from the edges. In short, the repulsive force from the edges of the lattice can be understood as that the skyrmions radial function wants to decay as slowly as possible; note that this radial function is classical and not a quantum mechanical wavefunction.
The skyrmion's spin-down (blue) part in Fig. 3.2 is only 4x4 spins. However, a rotation in the xy-components of the spins can be seen in a 12x12 sites area, and outside of that, the spins rotate in the opposite direction. This configuration is the fully relaxed configuration, the lowest energy state for the skyrmion. In such a configuration, the skyrmion presence is much more significant than expected by looking only at the central 4x4 spin-down part. When the skyrmion is forced towards the lower edge, it likely wants to return to the lower energy state in the center, in other words, to the state where there are some lattice sites between the skyrmion and the edge of the lattice.

Case 3: A larger impurity configuration

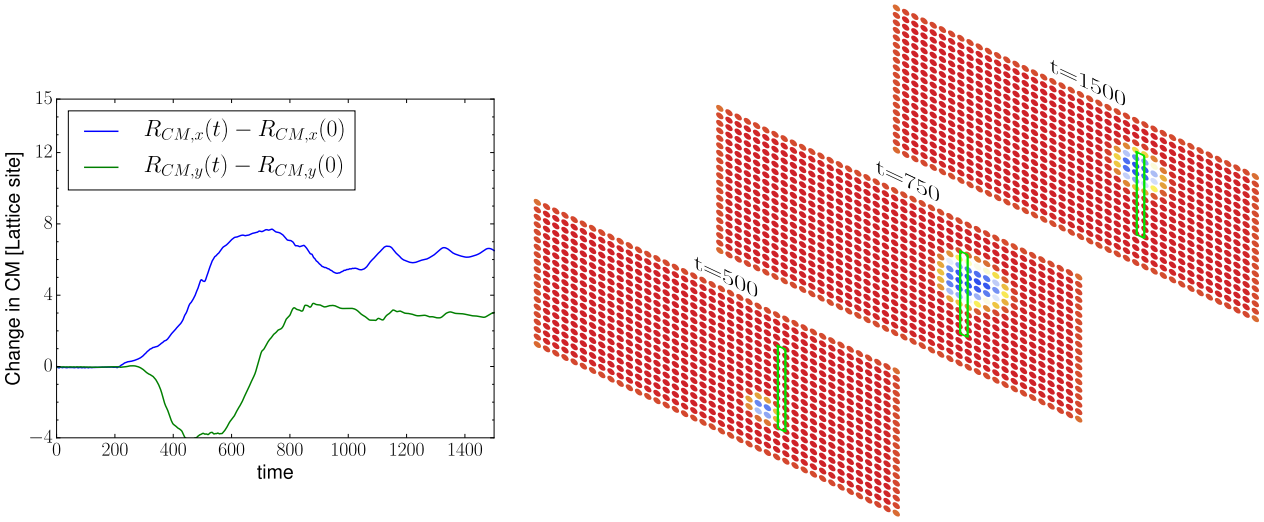

Figure 3.5: The center of mass movement of the skyrmion (left), and some snapshots of the z-component of the localized spins (right). We use $g = 1$, $\mathbf{B} = (0, 0, 0.05)$, $t_s = -1$, $K = 0.6$, $\alpha = 0.01$, $\alpha_R = 0$, $J = 0.5$, $D = 0.4$ (Bloch type), $\gamma = 0.1$, $\tau = 200$, $\mu = 0$ (start at half-filling) and $V = 2$. The color in the spins indicates the z-component red is $+1$ and blue is -1.

Fig.9, shows the skyrmion dynamics for the case of a "columnar" impurity that covers almost the whole lattice in the y-direction. Again the impurity is two lattice sites thick, and here, with four sites at the top and the bottom left unperturbed. The characteristic bump downwards in the y-component of the center of mass is also seen here, but it is twice as big as the ones seen in the previous cases.
As it can be seen in the center of mass movement in Fig. 3.5, the velocity in the y-direction is large before the skyrmion is halted. As a result, the skyrmion is very small in the snapshot at $t = 500$, which could indicate that it is almost annihilated. The return toward the center is most likely aided by the lower wall in this case. However, the impurity almost certainly also plays a role since we have seen that the skyrmion can not escape the impurity when it is inside.
After $t = 500$, the skyrmion recoils upwards, but the collision with the top does not seem as severe as in case 1. Likely, this is because the velocity is lower while the skyrmion is already stuck. Furthermore, for $t = 500$, it also looks like the skyrmion keeps moving in the x-direction. In the snapshot at $t = 750$, we can see that some movement is due to the skyrmion expanding to the right. However, at later times the skyrmion shrinks again to achieve its final position at $t = 1500$.

1.4 A new regime

In this subsection, we vary the bias V and use two different couplings γ in order to fully explore the skyrmion movement as a function of current. We consider the velocity as a marker for different regimes of skyrmion dynamics. However, a velocity only captures part of the picture of the movement of the skyrmion since, often in our simulations, the movement is far from a constant translation. The velocity is calculated by measuring the change in the center of mass of the skyrmion before it gets close to the boundary and dividing the distance by the time it to reach the boundary.

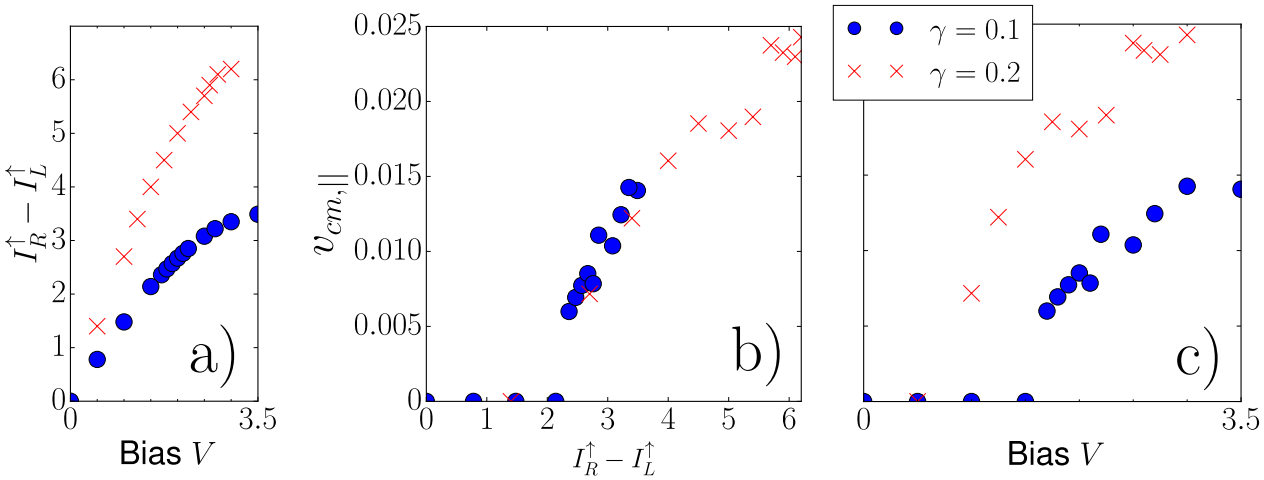

Figure 3.6: We use: $g = 1$, $\mathbf{B} = (0, 0, 0.05)$, $t_s = -1$, $K = 0.6$, $\alpha = 0.01$, $\alpha_R = 0$, $J = 0.5$, $D = 0.4$ (Bloch type), $\tau = 200$ and $\mu = 0$ (start at half-filling). In a) we plot current versus bias in the leads, b) show the center of mass velocity parallel to the current, and c) shows the center of mass velocity versus the bias in the leads.

Close to the boundary, there is a repulsive force on the skyrmion that prevents it from colliding; if we use a large current density, the velocity can be so large that the skyrmion collides with the wall and gets annihilated or sticks to the wall where it gets a topological charge of 1/2. However, before this happens, the large current could create other skyrmions. Now consider velocity dependence on current (Fig. 3.6b)). The switch from no movement at all to linear movement is expected from the LLG equation, where the point at which this happens could be related to the energies within the spin system compared to the force the itinerant electrons exert on the skyrmion. As the skyrmion moves a lattice site, it is temporarily in a higher energy state; if the force is too weak, it relaxes to the original lattice site, which is what we see for currents $j < j_c \sim 2$ (the small scale oscillations which we saw in the center of mass in Fig. 3.2 are consistent with this argument).

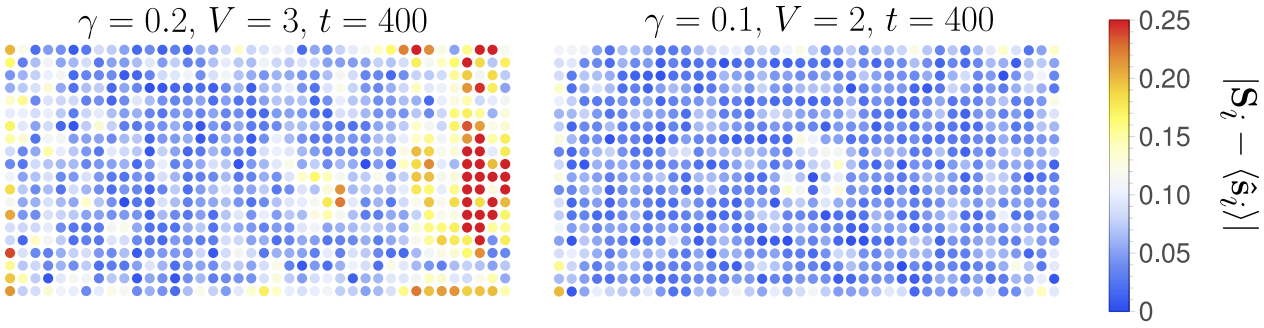

Figure 3.7: Difference between the spins of the itinerant electrons and the localized moments for a case within the linear regime and one in the non-linear regime. We use: $g = 1$, $\mathbf{B} = (0, 0, 0.05)$, $t_s = -1$, $K = 0.6$, $\alpha = 0.01$, $\alpha_R = 0$, $J = 0.5$, $D = 0.4$ (Bloch type), $\tau = 200$ and $\mu = 0$ (start at half-filling).

At some point, increasing the current in the system does not significantly increase the velocity at which the skyrmion moves. This signifies the breakdown of the adiabatic picture where the itinerant electron spin is aligned with the localized spins. In Fig. 3.7, we can see a much larger difference between localized and itinerant spins when we are in the non-linear regime. The assumption used to derive the linear current relation was that the coupling is strong enough that the spins of the itinerant electrons align with the spins of the localized moments. Unsurprisingly, we see that the formula fails when the assumption breaks down.

2 Characterization of the itinerant electrons

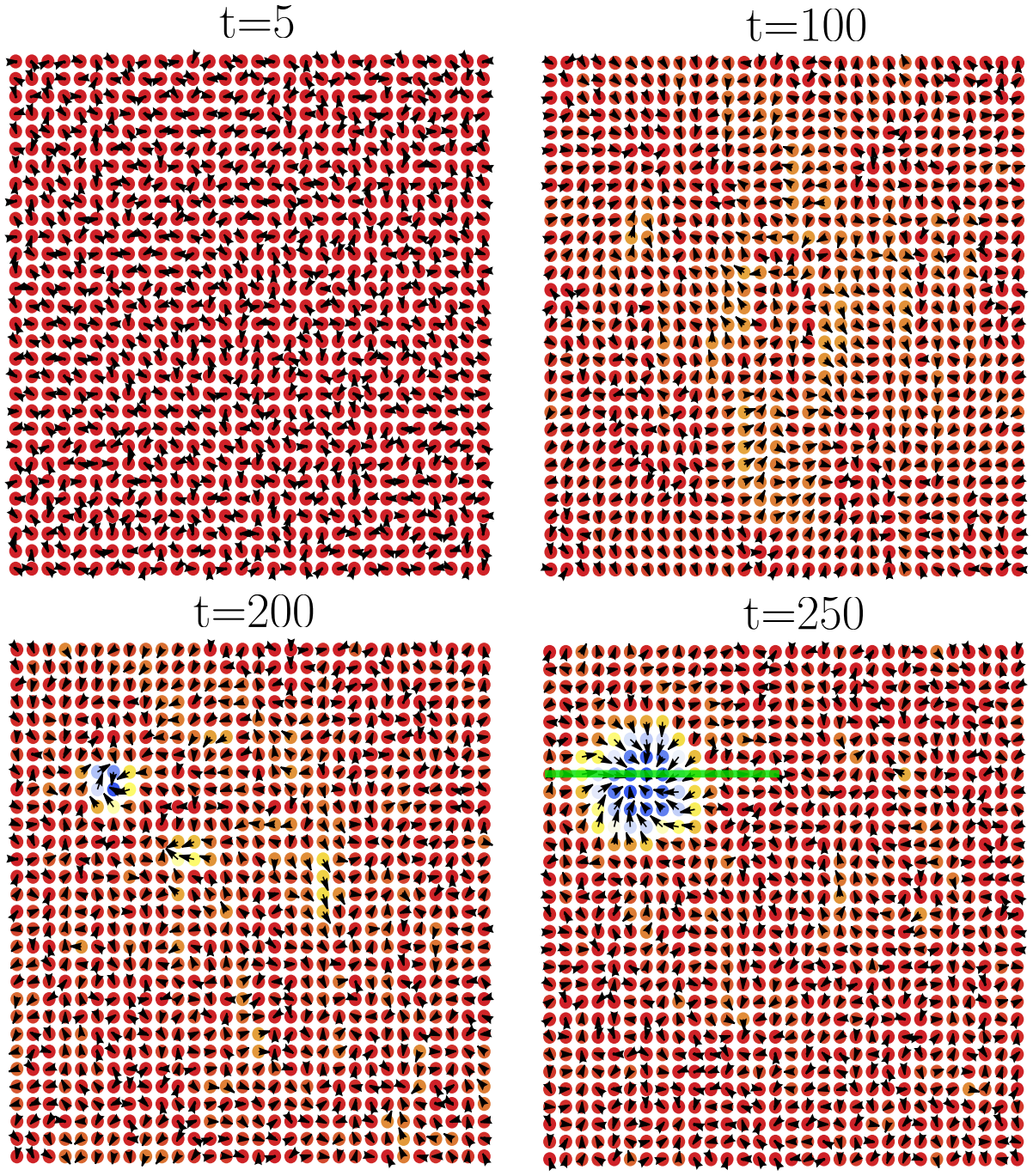

Figure 3.8: Snapshoots of the localized spins during the dynamics. The sites which are considered in the LDOS calculation are marked in green. $t_s = -1$, $\alpha_R = -0.5$, $g = 2.5$, $\mathbf{B} = (0, 0, 0.02)$, $K = 0$, $\alpha = 0$, $J = 0.1$, $D = 0.05$ (Néel type), $\gamma = 0$, $\mu = 0$ and the form of the laser is in Appendix 3. The color in the spins indicates the z-component red is $+1$ and blue is -1, and the arrows indicate the direction in the xy-plane.

So far, our focus has been largely on the spin dynamics associated with the skyrmion. However, it also very interesting to look closely at the behavior of the itinerant electrons and their spins. To this end, we turn to the case of skyrmion photocreation in a spin+electron system, first considered in [2]. There, it was shown that an efficient and fast mechanism for photocreation originates from the direct coupling between light and electrons in the presence of Rashba spin-orbit interaction. Not much attention was given to the characterization of the electron dynamics, something that we intend to address in the following. The indicators to qualify the behavior of the electrons will be the topological charge, the electronic local density of states, and the Chern number.
In this section, we use $\gamma = 0$ throughout since the leads could act as a dissipation source and reduce the chances of skyrmion nucleation. The laser is applied between $t = 0$ and $t = 90$, it has frequency $\omega = 0.5$, it is strongest in the center of the lattice, and it decays outwards with a Gaussian profile with $\sigma = 6$. The mathematical details are in Appendix 3; here, we focus on the behavior of the itinerant electrons. To minimize the effect of the boundary, periodic boundary conditions are used. Furthermore, we pick the parameters: $t_s = -1$, $\alpha_R = -0.5$, $g = 2.5$, $\mathbf{B} = (0, 0, 0.02)$, $K = 0$, $\alpha = 0$, $J = 0.1$, $D = 0.05$ (Néel type), $\gamma = 0$ and $\mu = 0$.

2.1 The topological charge

Due to the periodic boundary conditions, the topological charge is always an integer. Additionally, the strong Kondo coupling between the layers forces the spins to be very aligned, and hence a skyrmion is created in the localized moments immediately after one has been created in the itinerant electrons. Importantly, a skyrmion is created first in the itinerant electrons, which means that it is the localized spins that react to the itinerant spins.
Often charges are conserved in physics; however, it does not seem so in this case. If that is the case, a skyrmion of charge $+1$ is created in the localized moments after the skyrmion with charge -1 has been created in the itinerant electrons. If, on the other hand, we change the sign of the Kondo coupling to antiferromagnetic coupling, then the charge will be approximately conserved. Since the two textures will tend to anti-align, we get that $Q_{lo} + Q_{it} = 0$. However, as it is the case in Fig. 3.9, there will also be a transient time such that the charge is not perfectly conserved. However, the charge would be conserved over long time scales.

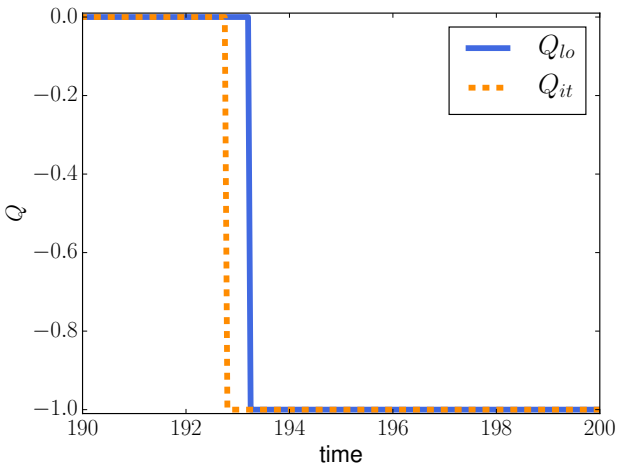

Figure 3.9: The topological charge for the itinerant and localized moments. $t_s = -1$, $\alpha_R = -0.5$, $g = 2.5$, $\mathbf{B} = (0, 0, 0.02)$, $K = 0$, $\alpha = 0$, $J = 0.1$, $D = 0.05$ (Néel type), $\gamma = 0$, $\mu = 0$ and the form of the laser is in Appendix 3.

2.2 Local density of states

The local density of states is directly accessible through scanning tunneling microscope experiments, and the results of this section could thus be experimentally tested. It may also be important to understand the density of states to engineer the itinerant electrons in skyrmion applications. Since skyrmions are on the scale of nanometers, local variations are expected to be non-negligible. We will see that the presence of a skyrmion drastically affects the local density of states.

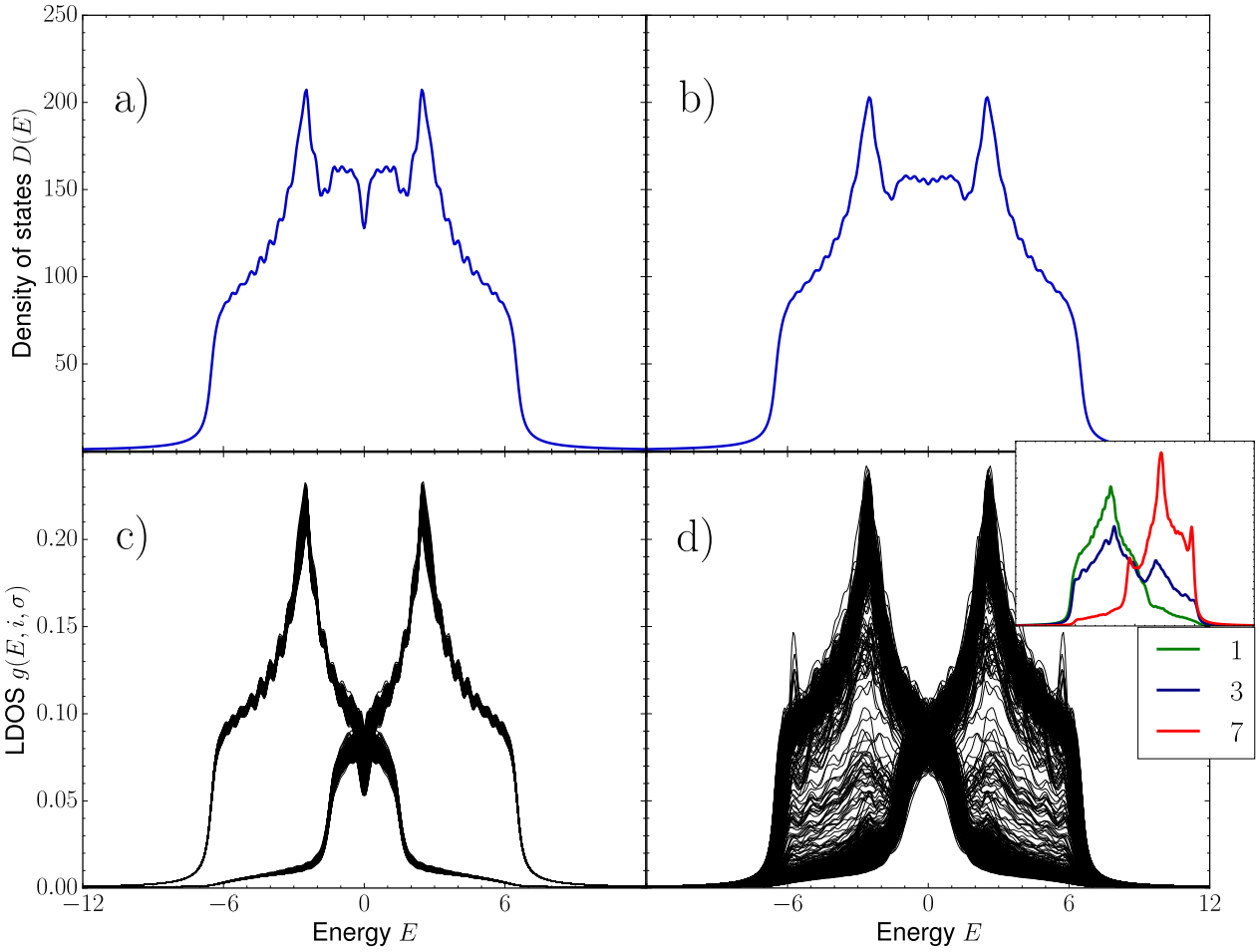

Figure 3.10: The LDOS and the DOS for two representative points in time. a) the DOS at $t = 5$, b) the DOS at $t = 250$, c) the LDOS at $t = 5$ for all sites and spin projections and d) LDOS at $t = 250$ for all sites and spin projections. The inset in d) shows the LDOS for the lattice sites $(x, y) = (1, 23)$,$(3, 23)$ and $(7, 23)$ with spin-up, which is indicated in Fig. 3.8 and above the heatmap in Fig. 3.11. We use the parameters $t_s = -1$, $\alpha_R = -0.5$, $g = 2.5$, $\mathbf{B} = (0, 0, 0.02)$ and the spin texture is given in Fig. 3.8.

In Fig. 3.10c), we can see that the local density of states does not vary much when we are in a ferromagnetic state. The local density of states essentially consists of the tight-binding result split up in two bands, one for spin-up and one for spin-down. The tight-binding result is what one gets if the model only had the hopping t_s, and the density of states, in that case,

is a sharp bump at $E = 0$. We get a splitting into two bumps because the localized moments act as a constant external field in the z-direction. The spin-up band is lower in energy and lies at an energy $-g$ since the electrons gain an energy g if they align with the localized moments. Likewise, the spin-down band lies at $+g$ since the electrons lose an energy g if they align with the localized moments.
When a skyrmion has been created, the spins are no longer spatially constant, in Fig. 3.10d) we can see that there is certainly much more variation in the local density of states than in 3.10c). To further understand the variation of the local density of state, we look at 15 lattice sites in the spin-up subspace.

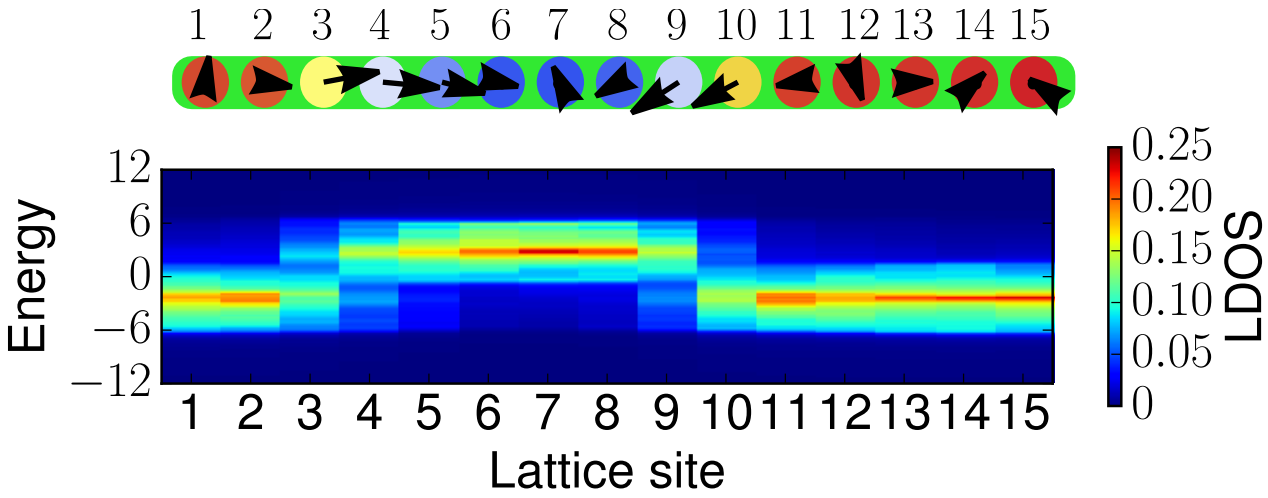

Figure 3.11: Local density of states for the lattice sites at $t = 250$ $x = 1, \ldots, 15$ and $y = 23$ with spin-up, which are shown above the heatmap and are indicated in Fig. 3.8d). $t_s = -1$, $\alpha_R = -0.5$,$g = 2.5$, $\mathbf{B} = (0, 0, 0.02)$ and the spin texture is also given in Fig. 3.8d).

The x-axis of the heatmap in Fig. 3.11 is discrete, whereas the y-axis is continuous. We can see that the local density of states at sites one and two essentially has a single band, i.e. we get the spin-up band as in Fig. 3.10c). Similarly, the sites after ten also have a single band; if we continued up to the last lattice site in the x-direction, we would still see the same local density of states since we are outside of the skyrmion. The sites in the skyrmion's center have a spin-down peak instead of the spin-up peak, which can be seen at sites 6-8. When going from inside to outside of the skyrmion, we see a mixing of the two bands, which can be seen in sites 3-5 and 9-10.

2.3 Chern number

A nonzero Chern number indicates a nontrivial k-space topology, analogous to a walk around a Möbius strip, where one ends up on the other side. In the present case, the walk is in k-space, and a nonzero Chern number indicates that a phase has been picked up during a cyclic adiabatic change of parameters. In this case, the Chern number is calculated for a single band in the bandstructure and thus indicates whether or not the bandstructure is topological. Due to the high computational cost, we only present the Chern number for a handful of points in time.

The skyrmion and the non-zero topological charge appear at $t \sim 190$, but we see a non-zero Chern number at $t \sim 90$. The emergence of the Chern number happens during the end of the laser pulse, which is sent into the system. Therefore, the laser has driven the system into a non-trivial state. One can imagine that the laser carried a non-trivial topology which was transferred to the system, but how to quantify this is not clear at this stage. The non-zero Chern number is temporarily lost until it re-appears at $t \sim 200$ again in the form of a skyrmion. Hence it appears as if the topological charge is not conserved, but this might be because not everything is considered. However, then we also need to answer where the charge goes between times $t = 125$ and $t = 190$, which could be explained by the Chern number going to other bands.

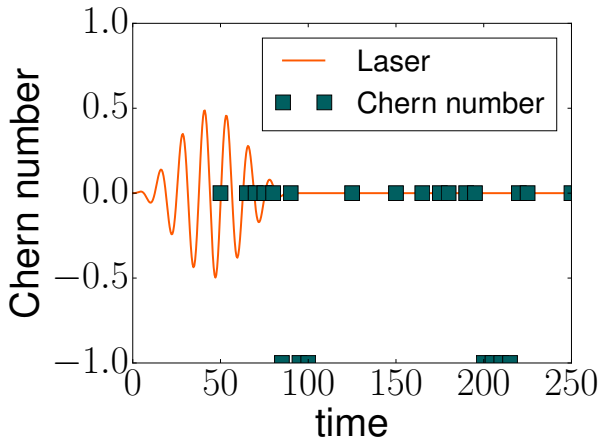

Figure 3.12: Chern number for the first excited state and the laser is drawn schematically. $t_s = -1$, $\alpha_R = -0.5$, $g = 2.5$, $\mathbf{B} = (0, 0, 0.02)$, $K = 0$, $\alpha = 0$, $J = 0.1$, $D = 0.05$ (Néel type), $\gamma = 0$, $\mu = 0$ and the form of the laser is in Appendix 3.

Strictly speaking, the Chern number is defined for a non-degenerate band; however, since the spins evolve with time, we have a Hamiltonian with a strong time dependence and, therefore, plenty of variation in the band structure. In addition, the bands cross; thus, to treat the problem rigorously, one would have to look at a subset of bands that only cross each other and no other bands after a particular time. A subset is hard to find in the present case since the bands show plenty of movement after the laser has been shone on the system. The Chern number is nevertheless an essential observable since it is directly related to the Hall conductance. The Hall conductance is the quantized conductance in the quantum Hall effect. Due to the non-zero Chern number, one could expect quantized conductance in a skyrmion system. However, it is hard to measure such conductance since the skyrmion will most likely move as a result of the current applied. One can have a better chance to measure the conductance in a skyrmion-crystal state, where the skyrmions are essentially locked in their place by other skyrmions (as in Fig. 1.2b)).

CHAPTER 4

Conclusion and outlook

In this thesis, we simulated magnetic skyrmions with a Kondo lattice Hamiltonian, where the localized movements are treated classically, and the itinerant electrons are treated quantum mechanically. The Kondo lattice is the central system that was coupled to metallic leads that represent a macroscopic environment. To deal with the embedding self-energy arising from the leads, it was necessary to develop a new approximation, which we call the non-interacting approximation.

The code developed allowed us to expand on previous results for a coupled spin-electron system [1, 2]. The first result was that we found a nonlinear regime for the skyrmion velocity as a function of current; such a regime is not considered in the literature to the best of the author's knowledge. The new regime is highly nonadiabatic and could lead to new unobserved skyrmion behaviors since experiments are typically in the linear regime. The new regime is characterized by a decoupling of the spins of the localized and itinerant electron, which is gradual in the finite system we have. However, if one goes to an infinite system, there could be a discontinuous decoupling, much like in a phase transition.

We have presented some representative results for skyrmion movement in the presence of impurities. To treat the disorder formally, one usually considers disorder averaging, which means that the average is taken over many different strengths and positions of the impurities. The averaging then gives the average effect of an impurity. We have considered only a few different types of impurities and all with the same strength, but it would be interesting to see what happens in general.

We have explored the itinerant electrons in some detail by looking at experimentally observable quantities, such as the local density of states. The local density of states is interesting since it can be probed directly in experiments. One further development is to go closer to experiment by picking parameters from a DFT calculation and including more terms in the Hamiltonian. An obvious improvement in that direction is to include interactions between the itinerant electrons, such as Coulomb interactions. These interactions could be included in the description without much effort with the second Born approximation, which is a good approximation when the magnitude of the interactions is small.

The code can deal with leads and a laser, a natural continuation is to set $\gamma \neq 0$. Skyrmion nucleation in the presence of the leads is interesting since this would be much closer to what happens in an actual experiment. One could imagine that the leads are detrimental to skyrmion nucleation, which could be the case since they act as a source of dissipation. However, the leads also act as a source of electrons which could help facilitate skyrmion creation. These questions will be continued to be explored after the project is finished.
In principle, skyrmions can also be created by a strong electric current, which is an additional interesting further development. We have seen such things in the simulations, i.e., when the current is considerable, there are many nonadiabatic effects, and a skyrmion is created. Sometimes it is stuck to the wall where the current was induced. Creation by a current is easier, but it could offer less control of the nucleation since it is expected that the skyrmion is created close to the leads. It is worth to point out here that an equally important scenario related to the creation of a skyrmion is when the latter is *destroyed* by light (i.e. skyrmion erasure). This is certainly within the scope of our approach.
The band structure is interesting not only from a fundamental perspective. To be able to engineer skyrmion applications, knowledge of the itinerant electrons is essential since it is often these which are manipulated directly. The phenomena in the localized spins only come as a secondary effect due to the interaction with the itinerant electrons. Such ideas warrant a further investigation of the band structure. The Chern number is calculated from the band structure, and a nonzero Chern number was found in some scenarios, indicating that the itinerant electrons are topological. However, we already knew this due to them having a nonzero topological charge. In the literature, there is little discussion of the conservation of charge since it is believed not to be the case in natural systems. Nevertheless, it could still be that some quantity is not taken into account, which would give a conserved charge. If there was charge conservation, this could have great theoretical and experimental consequences.

Bibliography

[1]E. Viñas Boström and C. Verdozzi, physica status solidi (b) **256**, 1800590 (2019).

[2]E. Viñas Boström, A. Rubio, and C. Verdozzi, npj Comput Mater **8** (2022).

[3]P. Hohenberg and W. Kohn, Phys. Rev. **136**, B864–B871 (1964).

[4]W. Kohn and L. J. Sham, Phys. Rev. **140**, A1133–A1138 (1965).

[5]J.-P. Joost, N. Schlünzen, and M. Bonitz, Physical Review B **101** (2020).

[6]R. Tuovinen, Y. Pavlyukh, E. Perfetto, and G. Stefanucci, arXiv:2211.15635 (2022).

[7]J. Kondo, Progress of Theoretical Physics **32**, 37–49 (1964).

[8]K. G. Wilson, Rev. Mod. Phys. **47**, 773–840 (1975).

[9]T. Jeong and W. E. Pickett, Phys. Rev. B **70**, 075114 (2004).

[10]S. Mühlbauer, B. Binz, F. Jonietz, C. Pfleiderer, A. Rosch, A. Neubauer, R. Georgii, and P. Böni, Science **323**, 915–919 (2009).

[11]F. Zheng, L. Kiselev N.S.and Yang, and et al, Nat. Phys. **18**, 863–868 (2022).

[12]K. Everschor-Sitte, J. Masell, R. M. Reeve, and M. Kläui, Journal of Applied Physics **124**, 240901 (2018).

[13]T. Moriya, Phys. Rev. **120**, 91–98 (1960).

[14]P. W. Anderson, Phys. Rev. **115**, 2–13 (1959).

[15]W. Koshibae, Y. Ohta, and S. Maekawa, Phys. Rev. B **47**, 3391–3400 (1993).

[16]D. Coffey, T. M. Rice, and F. C. Zhang, Phys. Rev. B **44**, 10112–10116 (1991).

[17]H.-P. Eckle, *Models of Quantum Matter: A First Course on Integrability and the Bethe Ansatz.* (Oxford University Press, 2019).

[18]S. L. Zhang, W. W. Wang, D. M. Burn, H. Peng, H. Berger, A. Bauer, C. Pfleiderer, G. van der Laan, and T. Hesjedal, Nature Communications **89**, 085131 (2018).

[19]J. Sampaio, V. Cros, S. Rohart, A. Thiaville, and A. Fert, Nature Nanotechnology **8**, 839–844 (2013).

[20]Y. B. Bazaliy, B. A. Jones, and S.-C. Zhang, Phys. Rev. B **57**, R3213–R3216 (1998).

[21]J. Zang, M. Mostovoy, J. H. Han, and N. Nagaosa, Phys. Rev. Lett. **107**, 136804 (2011).

[22]S. Huang, C. Zhou, G. Chen, H. Shen, A. K. Schmid, K. Liu, and Y. Wu, Phys. Rev. B **96**, 144412 (2017).

[23]Y. Luo, S.-Z. Lin, M. Leroux, N. Wakeham, D. M. Fobes, E. D. Bauer, J. B. Betts, J. D. Thompson, A. Migliori, M. Janoschek, and B. Maiorov, Communications Materials **1**, 83 (2020).

[24]J. Iwasaki, M. Mochizuki, and N. Nagaosa, Nature Communications **4**, 1463 (2013).

[25]J. Seidel, *Topological Structures in Ferroic Materials* (2016).

[26]A. A. Thiele, Phys. Rev. Lett. **30**, 230–233 (1973).

[27]D. Apalkov, A. Khvalkovskiy, S. Watts, V. Nikitin, X. Tang, D. Lottis, K. Moon, X. Luo, E. Chen, A. Ong, et al., ACM Journal on Emerging Technologies in Computing Systems (JETC) **9**, 1–35 (2013).

[28]T. Skyrme, Proc. R. Soc. Lond. A **260**, 127–138 (1961).

[29]T. Skyrme, Nucl. Phys. **31**, 556–569 (1962).

[30]V. Pokrovsky, Advances in Physics **28**, 595–656 (1979).

[31]A. Bogdanov and A. Hubert, Journal of Magnetism and Magnetic Materials **138**, 255–269 (1994).

[32]X. Z. Yu, Y. Onose, and N. Kanazawa, Nature **465**, 901–904 (2010).

[33]M. Ezawa, Phys. Rev. Lett. **105**, 197202 (2010).

[34]T.-H. Kim, H. Zhao, B. Xu, B. A. Jensen, A. H. King, M. J. Kramer, C. Nan, L. Ke, and L. Zhou, Nano Letters **20**, 4731–4738 (2020).

[35]B. Berg and M. Lüscher, Nuclear Phys. B **190**, 412–424 (1981).

[36]N. Nagaosa and Y. Tokura, Nature Nanotechnology **8**, 899–911 (2013).

[37]J. Fröhlich, A. Knowles, and E. Lenzmann, Letters in Mathematical Physics **82**, 275–296 (2007).

[38]E. H. Lieb, Communications in Mathematical Physics **31**, 327–340 (1973).

[39]Y. Meir and N. S. Wingreen, Phys. Rev. Lett. **68**, 2512–2515 (1992).

[40]A.-P. Jauho, N. S. Wingreen, and Y. Meir, Phys. Rev. B **50**, 5528–5544 (1994).

[41]J. J. Sakurai and J. Napolitano, *Modern Quantum Mechanics (2nd ed.)* (2017).

[42]B. M. Victor, Proc. R. Soc. Lond. **392**, 45–57 (1984).

[43]G. Stefanucci and R. A. van Leeuwen, *Nonequilibrium many-body theory of quantum systems: a modern introduction* (Cambridge University Press, 2013).

[44]L. P. Kadanoff and G. Baym, *Quantum statistical mechanics : green's function methods in equilibrium and nonequilibrium problems* (W.A. Benjamin, 1962).

[45]P. Lipavský, V. Špička, and B. Velický, Physical Review B **34**, 6933–6942 (1986).

[46]S. Latini, E. Perfetto, A.-M. Uimonen, R. van Leeuwen, and G. Stefanucci, Phys. Rev. B **89**, 075306 (2014).

[47]A. Kalvová, B. Velický, and V. Špička, Europhysics Letters **121**, 67002 (2018).

[48]P. Myöhänen, A. Stan, G. Stefanucci, and R. van Leeuwen, Europhysics Letters **84**, 67001 (2008).

[49]E. Perfetto, G. Stefanucci, and M. Cini, Phys. Rev. Lett. **105**, 156802 (2010).

[50]R. Tuovinen, E. Perfetto, G. Stefanucci, and R. van Leeuwen, Phys. Rev. B **89**, 085131 (2014).

[51]N. Schlünzen, K. Balzer, H. Ohldag, J.-P. Joost, and M. Bonitz, arXiv:2211.09615 (2022).

[52]M. Ridley, A. MacKinnon, and L. Kantorovich, Phys. Rev. B **91**, 125433 (2015).

[53]P. Depondt and F. G. Mertens, Journal of Physics: Condensed Matter **21**, 336005 (2009).

CHAPTER 5

Appendix

1 Full WBL derivation

The embedding self-energy is

$$\Sigma^{\text{emb}} = \sum_{\alpha} \Sigma^{\alpha} = \sum_{\alpha} h_{M\alpha}(z) G_{\alpha\alpha}(z,\bar{z}) h_{\alpha M}(\bar{z}) \tag{S.1.1}$$

The connection between system M and environment is just the hopping

$$t_l(z) \sum_{\sigma} \sum_{i_y=1}^{N_y} \Big[a^{\dagger}_{1_x i_y \sigma l} c_{1_x i_y \sigma} + a^{\dagger}_{1_x i_y \sigma l} c_{N_x i_y \sigma} + h.c. \Big]. \quad t_l(z) = t_l \sin(z\pi/(2\tau)) \tag{S.1.2}$$

$$h_{\alpha\alpha}(z) = -t \sum_{\langle ij \rangle} a_i^{\dagger} a_j + \sum_i (V(z) + \mu) a_i^{\dagger} a_i \tag{S.1.3}$$

the environment GF is non-interacting, hence it can be written on the form [43]

$$G_{\alpha\alpha}(z,\bar{z}) = -i\mathcal{T}\Big\{ e^{-i\int_{t_0}^{z} h_{\alpha\alpha}(x)\mathrm{d}x} \Big\} \big[\theta(z,\bar{z}) \bar{f}(h^M_{\alpha\alpha}) - \theta(\bar{z},z) f(h^M_{\alpha\alpha}) \big] \bar{\mathcal{T}}\Big\{ e^{i\int_{t_0}^{\bar{z}} h_{\alpha\alpha}(x)\mathrm{d}x} \Big\} \tag{S.1.4}$$

$$= -i\mathcal{T}\Big\{ e^{it\sum_{\langle ij \rangle} a_i^{\dagger} a_j (z - t_0)} e^{-i\int_{t_0}^{z} (V_\alpha(x) + \mu)\mathrm{d}x} \Big\} \big[\theta(z,\bar{z}) \bar{f}(h^M_{\alpha\alpha}) - \theta(\bar{z},z) f(h^M_{\alpha\alpha}) \big] \tag{S.1.5}$$

$$\bar{\mathcal{T}}\Big\{ e^{-it\sum_{\langle ij \rangle} a_i^{\dagger} a_j (\bar{z} - t_0)} e^{i\int_{t_0}^{\bar{z}} (V_\alpha(x) + \mu)\mathrm{d}x} \Big\} \tag{S.1.6}$$

The tight-binding Hamiltonians can be diagonalized by a fourier-transform

$$[G_{\alpha\alpha}(z,\bar{z})]_{kk'} = -i\delta_{kk'} \mathcal{T}\Big\{ e^{-i\epsilon_{k\alpha}(z - t_0)} e^{-i\int_{t_0}^{z} (V_\alpha(x) + \mu)\mathrm{d}x} \Big\} \big[\theta(z,\bar{z}) \bar{f}(\epsilon_{k\alpha}) - \theta(\bar{z},z) f(\epsilon_{k\alpha}) \big] \tag{S.1.7}$$

$$\bar{\mathcal{T}}\Big\{ e^{i\epsilon_{k\alpha}(\bar{z} - t_0)} e^{i\int_{t_0}^{\bar{z}} (V_\alpha(x) + \mu)\mathrm{d}x} \Big\} \tag{S.1.8}$$

$$= -i\delta_{kk'} e^{-i\epsilon_{k\alpha}(z - \bar{z}) - i\int_{\bar{z}}^{z} (V_\alpha(x) + \mu)\mathrm{d}x} \big[\theta(z,\bar{z}) \bar{f}(\epsilon_{k\alpha}) - \theta(\bar{z},z) f(\epsilon_{k\alpha}) \big] \tag{S.1.9}$$

$$\tag{S.1.10}$$

Consider the matrix-form of the embedding self-energy introduce real-space basis a, b and momentum-space basis p, k

$$\Sigma_{ij}^{\alpha} = \langle i| \sum_{abkp} h_{M\alpha}(z) \, |a\rangle\langle a| \, |p\rangle\langle p| \, G_{\alpha\alpha}(z,\bar{z}) \, |k\rangle\langle k| \, |b\rangle\langle b| \, h_{\alpha M}(\bar{z}) \, |j\rangle \tag{S.1.11}$$

$$= \sum_{abk} [h_{M\alpha}(z)]_{ia} \, \langle a|k\rangle \, [G_{\alpha\alpha}(z,\bar{z})]_{kk} \, \langle k|b\rangle \, [h_{\alpha M}(\bar{z})]_{bj} \tag{S.1.12}$$

$$= \sum_{abk} [t_l(z)\delta_{i_x\alpha_c}\delta_{i_y a_y}\delta_{1a_x}]_{ia} \, \langle a|k\rangle \, [G_{\alpha\alpha}(z,\bar{z})]_{kk} \, \langle k|b\rangle \, [t_l(\bar{z})\delta_{j_x\alpha_c}\delta_{j_y b_y}\delta_{1b_x}]_{bj} \tag{S.1.13}$$

$$= \delta_{i_x\alpha_c}\delta_{j_x\alpha_c} \sin(z\pi/2\tau)\sin(\bar{z}\pi/2\tau) t_l^2 \sum_{k} \langle 1 i_y|k\rangle \, [G_{\alpha\alpha}(z,\bar{z})]_{kk} \, \langle k|1 j_y\rangle \tag{S.1.14}$$

one can show that the eigenstates of the 2D tight-binding Hamiltonian with open boundary conditions is

$$|k\rangle = \sqrt{\frac{2}{N_x+1}}\sqrt{\frac{2}{N_y+1}} \sum_{i_x=1}^{N_x}\sum_{i_y=1}^{N_y} \sin\left(\frac{\pi k_x i_x}{N_x+1}\right)\sin\left(\frac{\pi k_y i_y}{N_y+1}\right)|i\rangle \tag{S.1.15}$$

This gives

$$\Sigma_{ij}^{\alpha} = \delta_{i_x\alpha_c}\delta_{j_x\alpha_c} \sin(z\pi/2\tau)\sin(\bar{z}\pi/2\tau) t_l^2 \frac{2}{N_x+1}\frac{2}{N_y+1} \tag{S.1.16}$$

$$\sum_{k} \sin^2\left(\frac{\pi k_x}{N_x+1}\right)\sin\left(\frac{\pi k_y i_y}{N_y+1}\right)\sin\left(\frac{\pi k_y j_y}{N_y+1}\right)[G_{\alpha\alpha}(z,\bar{z})]_{kk} \tag{S.1.17}$$

We now consider the relevant components of the self-energy.

$$[\Sigma_{ij}^{\alpha}]^{<} = \delta_{i_x\alpha_c}\delta_{j_x\alpha_c} \sin(z\pi/2\tau)\sin(\bar{z}\pi/2\tau) t_l^2 \frac{2}{N_x+1}\frac{2}{N_y+1} \tag{S.1.18}$$

$$\sum_{k} \sin^2\left(\frac{\pi k_x}{N_x+1}\right)\sin\left(\frac{\pi k_y i_y}{N_y+1}\right)\sin\left(\frac{\pi k_y j_y}{N_y+1}\right)[G_{\alpha\alpha}(z,\bar{z})]^{<}_{kk} \tag{S.1.19}$$

$$= i\delta_{i_x\alpha_c}\delta_{j_x\alpha_c} \sin(z\pi/2\tau)\sin(\bar{z}\pi/2\tau) t_l^2 \frac{2}{N_x+1}\frac{2}{N_y+1} \tag{S.1.20}$$

$$\sum_{k_x k_y} \sin^2\left(\frac{\pi k_x}{N_x+1}\right)\sin\left(\frac{\pi k_y i_y}{N_y+1}\right)\sin\left(\frac{\pi k_y j_y}{N_y+1}\right)\theta(\bar{z}-z) e^{-i\epsilon_{k\alpha}(z-\bar{z}) - i\int_{\bar{z}}^{z}(V_\alpha(x)+\mu)\mathrm{d}x} f(\epsilon_{k\alpha}) \tag{S.1.21}$$

We have a finite width of the strip, however, the leads extend to infinity in x-direction, hence $k_x\pi/(N_x+1)$ can be treated as a continuous variable.

$$[\Sigma_{ij}^{\alpha}]^{<} = \theta(\bar{z}-z) i\delta_{i_x\alpha_c}\delta_{j_x\alpha_c} \sin(z\pi/2\tau)\sin(\bar{z}\pi/2\tau) t_l^2 \frac{2}{N_y+1} \tag{S.1.22}$$

$$\sum_{k_y} \sin\left(\frac{\pi k_y i_y}{N_y+1}\right)\sin\left(\frac{\pi k_y j_y}{N_y+1}\right) e^{-i\int_{\bar{z}}^{z}(V_\alpha(x)+\mu)\mathrm{d}x} \frac{1}{\pi}\int_0^{\pi} \mathrm{d}\theta \sin^2(\theta) e^{-i\epsilon_{k\alpha}(z-\bar{z})} f(\epsilon_{k\alpha}) \tag{S.1.23}$$

change variables to $\epsilon_{k\alpha} = -2t_b\cos\theta - 2t_b\cos\left(\frac{\pi k_y}{N_y+1}\right) = \epsilon_{k_y} - 2t_b\cos\theta$, call it ϵ

$$[\Sigma^\alpha_{ij}]^< = \theta(\bar{z}-z)i\delta_{i_x\alpha_c}\delta_{j_x\alpha_c}\sin(z\pi/2\tau)\sin(\bar{z}\pi/2\tau)t_l^2\frac{2}{N_y+1}\sum_{k_y}\sin\left(\frac{\pi k_y i_y}{N_y+1}\right)\sin\left(\frac{\pi k_y j_y}{N_y+1}\right)$$

(S.1.24)

$$e^{-i\int_{\bar{z}}^{z}(V_\alpha(x)+\mu)\mathrm{d}x}\frac{1}{\pi}\int_{\epsilon_{k_y}-2t_b}^{\epsilon_{k_y}+2t_b}\frac{1}{2t_b}\sin(\theta)e^{-i\epsilon(z-\bar{z})}f(\epsilon)\mathrm{d}\epsilon \tag{S.1.25}$$

$$= \theta(\bar{z}-z)i\delta_{i_x\alpha_c}\delta_{j_x\alpha_c}\sin(z\pi/2\tau)\sin(\bar{z}\pi/2\tau)t_l^2\frac{2}{N_y+1} \tag{S.1.26}$$

$$\sum_{k_y}\sin\left(\frac{\pi k_y i_y}{N_y+1}\right)\sin\left(\frac{\pi k_y j_y}{N_y+1}\right)e^{-i\int_{\bar{z}}^{z}(V_\alpha(x)+\mu)\mathrm{d}x}\frac{1}{\pi}\int_{\epsilon_{k_y}-2t_b}^{\epsilon_{k_y}+2t_b}\underbrace{\frac{1}{2t_b}\sqrt{1-\left(\frac{\epsilon_{k_y}-\epsilon}{2t_b}\right)^2}}_{\rho(\epsilon)}e^{-i\epsilon(z-\bar{z})}f(\epsilon)\mathrm{d}\epsilon$$

(S.1.27)

(S.1.28)

take the WBL $t_b \to \infty$ while $\gamma = t_l^2/t_b$ is fixed, physically we assume that the local density of states at the first site $\rho(\epsilon)$ is constant hence $\rho(0) = 1/(2t_b)$ is used.

$$[\Sigma^\alpha_{ij}]^< = \theta(\bar{z}-z)i\delta_{i_x\alpha_c}\delta_{j_x\alpha_c}\sin(z\pi/2\tau)\sin(\bar{z}\pi/2\tau)\gamma\frac{2}{N_y+1} \tag{S.1.29}$$

$$\sum_{k_y}\sin\left(\frac{\pi k_y i_y}{N_y+1}\right)\sin\left(\frac{\pi k_y j_y}{N_y+1}\right)e^{-i\int_{\bar{z}}^{z}(V_\alpha(x)+\mu)\mathrm{d}x}\frac{1}{2\pi}\int_{-\infty}^{\infty}e^{-i\epsilon(z-\bar{z})}f(\epsilon)\mathrm{d}\epsilon \tag{S.1.30}$$

$$= i\frac{[\Gamma_\alpha]_{ij}}{2\pi}\theta(\bar{z}-z)\int_{-\infty}^{\infty}e^{-i\epsilon(z-\bar{z})}f(\epsilon)\mathrm{d}\epsilon \tag{S.1.31}$$

The retarded environment GF is given by

$$[G_{\alpha\alpha}(z,\bar{z})]^R_{kk'} = -\theta(z-\bar{z})i\delta_{kk'}e^{-i\epsilon_{k\alpha}(z-\bar{z})-i\int_{\bar{z}}^{z}(V_\alpha(x)+\mu)\mathrm{d}x} \tag{S.1.32}$$

We can follow the same procedure as for the lesser self-energy to get

$$[\Sigma^\alpha_{ij}]^R = -\theta(z-\bar{z})i\delta_{i_x\alpha_c}\delta_{j_x\alpha_c}\sin(z\pi/2\tau)\sin(\bar{z}\pi/2\tau)\gamma\frac{2}{N_y+1} \tag{S.1.33}$$

$$\sum_{k_y}\sin\left(\frac{\pi k_y i_y}{N_y+1}\right)\sin\left(\frac{\pi k_y j_y}{N_y+1}\right)e^{-i\int_{\bar{z}}^{z}(V_\alpha(x)+\mu)\mathrm{d}x}\frac{1}{2\pi}\int_{-\infty}^{\infty}e^{-i\epsilon(z-\bar{z})}\mathrm{d}\epsilon \tag{S.1.34}$$

$$= -i\delta_{i_x\alpha_c}\delta_{j_x\alpha_c}\sin(z\pi/2\tau)\sin(\bar{z}\pi/2\tau)\gamma\frac{2}{N_y+1} \tag{S.1.35}$$

$$\sum_{k_y}\sin\left(\frac{\pi k_y i_y}{N_y+1}\right)\sin\left(\frac{\pi k_y j_y}{N_y+1}\right)e^{-i\int_{\bar{z}}^{z}(V_\alpha(x)+\mu)\mathrm{d}x}\frac{1}{2}\delta(z-\bar{z}) \tag{S.1.36}$$

$$= -i\sin^2(z\pi/2\tau)\frac{[\Gamma_\alpha]_{ij}}{2}\delta(z-\bar{z}) \tag{S.1.37}$$

The WBL matrix is given by

$$[\Gamma^{\alpha}]_{ij}^{\sigma\sigma'} = \gamma\delta_{\alpha_c i_x}\delta_{\alpha_c j_x}\delta_{\alpha_s\sigma'}\delta_{\alpha_s\sigma}\sum_{k_y}\frac{4}{N_y+1}\sin\left(\frac{\pi k_y i_y}{N_y+1}\right)\times\sin\left(\frac{\pi k_y j_y}{N_y+1}\right) \tag{S.1.38}$$

The alpha label contains coordinate $\alpha_c = 1, N$ indices, N is the rightmost site. Here we have included spin $\alpha_s =\uparrow,\downarrow$, this is the only place the spin enters, the spin subspaces are decoupled within the leads.
There is one integral which needs to be evaluated in order to get the analytical expression for the lesser self-energy. Here we write t instead of $t - t'$ for brevity.

$$I^{<} = \int_{-\infty}^{\infty} d\epsilon\, f(\epsilon-\mu)e^{-i\epsilon t} = \int_{-\infty}^{\infty} d\epsilon\,\frac{1}{1+e^{\beta(\epsilon-\mu)}}e^{-i\epsilon t} = \int_{-\infty}^{\infty} d\epsilon\,\frac{1}{1+e^{\beta(\epsilon-\mu)}}e^{-i\epsilon t}e^{\eta\epsilon}$$

Close contour in lower half plane since $t < 0$, write $\tilde{t} = t + i\eta$. The poles are at $\beta(\epsilon_n - \mu) = -i\pi - 2\pi i n$ with $n \in \mathbb{Z}$

$$\begin{aligned} I^{<} &= -2\pi i\sum_{n=0}^{\infty} e^{-i\epsilon_n\tilde{t}}\mathrm{Res}\left[\frac{1}{1+e^{\beta(\epsilon_n-\mu)}}\right] = 2\pi i/\beta\sum_{n=0}^{\infty} e^{-(\pi+i\mu\beta+2\pi n)\tilde{t}/\beta} \\ &= 2\pi i/\beta e^{-\pi\tilde{t}/\beta - i\mu\tilde{t}}\sum_{n=0}^{\infty} e^{-2\pi n\tilde{t}/\beta} = 2\pi i/\beta e^{-\pi\tilde{t}/\beta-i\mu\tilde{t}}\frac{1}{1-e^{-2\pi\tilde{t}/\beta}} = e^{-i\mu\tilde{t}}\frac{i\pi/\beta}{\sinh\big(\pi\tilde{t}/\beta\big)} \end{aligned}$$

$$\begin{aligned} \mathrm{Res}\left[\frac{1}{1+e^{\beta(\epsilon_n-\mu)}}\right] &= \lim_{\epsilon\to i/\beta(\pi+2\pi n)+\mu}\frac{(\epsilon-(\pi+2\pi n)i/\beta+\mu)}{1+e^{\beta(\epsilon-\mu)}} = \lim_{\epsilon\to i/\beta(\pi+2\pi n)}\frac{(\epsilon-(\pi+2\pi n)i/\beta)}{1+e^{\beta\epsilon}} \\ &= \lim_{x\to 0}\frac{i/\beta x}{1+e^{i(x+\pi)}} = \lim_{x\to 0}\frac{i/\beta x}{1-(1+(ix)+\mathcal{O}((ix)^2))} = -1/\beta \end{aligned}$$

To generalize this result we consider the behavior for t close to 0.

$$e^{-i\mu\tilde{t}}\frac{i\pi/\beta}{\sinh\big(\pi\tilde{t}/\beta\big)} = e^{-i\mu\tilde{t}}\frac{i\pi/\beta}{\pi\tilde{t}/\beta+\mathcal{O}\big((\pi\tilde{t}/\beta)^2\big)} \to \mathcal{P}\left\{\frac{ie^{-i\mu t}}{t}\right\} + \pi\delta(t) \tag{S.1.39}$$

Hence

$$I^{<} = \mathcal{P}\left\{e^{-i\mu t}\frac{i\pi/\beta}{\sinh(\pi t/\beta)}\right\} + \pi\delta(t)$$

Since this is an integral coming from the lesser self-energy it is multiplied by $\theta(t)$, which means that in total we have:

$$\mathcal{P}\left\{e^{-i\mu t}\frac{i\pi/\beta}{\sinh(\pi t/\beta)}\right\} + \delta(t)\pi/2$$

The low temperature limit is then

$$\mathcal{P}\left\{\frac{ie^{-i\mu t}}{t}\right\} + \delta(t)\pi/2 \qquad \text{when } \beta\to\infty$$

$\theta(t)\delta(t)$ gives $\delta(t)/2$, since

$$\begin{aligned}\int_{-\infty}^{\infty} d\epsilon\, \theta(t) e^{-i\epsilon t} &= \int_{-\infty}^{\infty} d\epsilon \left(-\frac{1}{2\pi i}\int_{-\infty}^{\infty} d\epsilon'\, \frac{1}{\epsilon' + i\eta}\right) e^{-i\epsilon' t} e^{-i\epsilon t} = -\frac{1}{2\pi i}\int_{-\infty}^{\infty} d\epsilon \int_{-\infty}^{\infty} d\epsilon'\, e^{-i\epsilon t} \frac{1}{\epsilon' + i\eta} e^{-i\epsilon' t} \\ &= -\frac{1}{2\pi i}\int_{-\infty}^{\infty} d\epsilon \left(-i\pi e^{-i\epsilon t} + \mathcal{P}\int_{-\infty}^{\infty} d\epsilon' \left(\frac{1}{\epsilon'}\right) e^{-i(\epsilon'+\epsilon)t}\right) \\ &= \frac{1}{2}\int_{-\infty}^{\infty} d\epsilon e^{i\epsilon t} - \frac{1}{2\pi i}\int_{-\infty}^{\infty} d\epsilon\, \mathcal{P}\left\{\int_{-\infty}^{\infty} dx \frac{e^{-ixt}}{x - \epsilon}\right\} = \pi\delta(t)\end{aligned}$$

The second integral is the Hilbert transform e^{-ixt} in x, if $t \neq 0$ then the Hilbert transform is $i\mathrm{sgn}(t)e^{-i\epsilon t}$ which gives $\sim \delta(t)$ when integrated with ϵ and therefore it is zero. If $t = 0$ we have the Hilbert transform of a constant, hence it's again zero.

2 Approximation derivation

In the main text it is claimed that an integral on the following form gives a time-linear evolution:

$$\int_{t_0}^{t} \mathrm{d}\bar{t} \sum_{\alpha} e^{-i\int_{t}^{\bar{t}} V_\alpha(\tilde{t})\mathrm{d}\tilde{t}} \Lambda_\alpha(t-\bar{t}) s(t) s(\bar{t}) G^0(t-\bar{t}) \tag{S.2.1}$$

$$= s(t) \sum_{\alpha} \int_{t_0}^{t} \mathrm{d}\bar{t}\, e^{-i\int_{t}^{\bar{t}} V_\alpha(\tilde{t})\mathrm{d}\tilde{t}} \Lambda_\alpha(t-\bar{t}) s(\bar{t}) G^0(t-\bar{t}) = s(t) \sum_{\alpha} I_\alpha(t) \tag{S.2.2}$$

$$I_\alpha(t) = \int_{t_0}^{\tau} \mathrm{d}\bar{t}\, e^{-i\int_{t}^{\bar{t}} V_\alpha(\tilde{t})\mathrm{d}\tilde{t}} \Lambda_\alpha(t-\bar{t}) s(\bar{t}) G^0(t-\bar{t}) + \int_{\tau}^{t} \mathrm{d}\bar{t}\, e^{-i\int_{t}^{\bar{t}} V_\alpha(\tilde{t})\mathrm{d}\tilde{t}} \Lambda_\alpha(t-\bar{t}) s(\bar{t}) G^0(t-\bar{t}) \tag{S.2.3}$$

$$= \int_{t_0}^{\tau} \mathrm{d}\bar{t}\, e^{-iV_\alpha(t-\bar{t})} \Lambda_\alpha(t-\bar{t}) \sin(\pi\bar{t}/2\tau)^2 G^0(t-\bar{t}) + \int_{\tau}^{t} \mathrm{d}\bar{t}\, e^{-iV_\alpha(t-\bar{t})} \Lambda_\alpha(t-\bar{t}) G^0(t-\bar{t}) \tag{S.2.4}$$

$$= I_{\alpha,1}(t) + I_{\alpha,2}(t) \tag{S.2.5}$$

$$I_{\alpha,1} = \int_{t_0}^{\tau} \mathrm{d}\bar{t}\, e^{-iV_\alpha(t-\bar{t})} \Lambda_\alpha(t-\bar{t}) \left(\frac{1}{2} - \frac{1}{4} e^{-i\pi\bar{t}/\tau} - \frac{1}{4} e^{i\pi\bar{t}/\tau} \right) G^0(t-\bar{t}) = \frac{1}{2} I^0_{\alpha,1} - \frac{1}{4} I^+_{\alpha,1} - \frac{1}{4} I^-_{\alpha,1} \tag{S.2.6}$$

$$I^\Omega_{\alpha,1}(t+\Delta) = \int_{t_0}^{\tau} \mathrm{d}\bar{t}\, e^{-iV_\alpha(t+\Delta-\bar{t})} \Lambda_\alpha(t+\Delta-\bar{t}) e^{i\Omega\pi\bar{t}/\tau} G^0(t+\Delta-\bar{t}) \tag{S.2.7}$$

$$= \int_{t_0-\Delta}^{\tau-\Delta} \mathrm{d}y e^{-iV_\alpha(t-y)} \Lambda_\alpha(t-y) e^{i\Omega\pi(y+\Delta)/\tau} G^0(t-y) \tag{S.2.8}$$

$$= \left(\int_{t_0-\Delta}^{t_0} + \int_{t_0}^{\tau} - \int_{\tau-\Delta}^{\tau} \right) \mathrm{d}y\, e^{-iV_\alpha(t-y)} \Lambda_\alpha(t-y) e^{i\Omega\pi(y+\Delta)/\tau} G^0(t-y) \tag{S.2.9}$$

$$= e^{i\Omega\Delta/\tau} I^\Omega_{\alpha,1}(t) + \left(\int_{t_0-\Delta}^{t_0} - \int_{\tau-\Delta}^{\tau} \right) \mathrm{d}y\, e^{-iV_\alpha(t-y)} \Lambda_\alpha(t-y) e^{i\Omega\pi(y+\Delta)/\tau} G^0(t-y) \tag{S.2.10}$$

$$\approx e^{i\Omega\Delta/\tau} I^\Omega_{\alpha,1}(t) + \frac{\Delta}{2} \Bigg[e^{-iV_\alpha(t-t_0+\Delta)} \Lambda_\alpha(t-t_0+\Delta) e^{i\Omega\pi(t_0)/\tau} G^0(t-t_0+\Delta) \tag{S.2.11}$$

$$+ e^{-iV_\alpha(t-t_0)} \Lambda_\alpha(t-t_0) e^{i\Omega\pi(t_0+\Delta)/\tau} G^0(t-t_0) \Bigg] \tag{S.2.12}$$

$$- \frac{\Delta}{2} \Bigg[e^{-iV_\alpha(t-\tau+\Delta)} \Lambda_\alpha(t-\tau+\Delta) e^{i\Omega\pi(\tau)/\tau} G^0(t-\tau+\Delta)) \tag{S.2.13}$$

$$+ e^{-iV_\alpha(t-\tau)} \Lambda_\alpha(t-\tau) e^{i\Omega\pi(\Delta+\tau)/\tau} G^0(t-\tau) \Bigg] \tag{S.2.14}$$

So we need to evolve two GF:s, $G^0(t-t_0)$ and $G^0(t-\tau)$. The second one is only needed when $t>\tau$, since before then this integral is up to $t+\Delta$ and the change of variables on gives one new interval instead of two.

$$I_{\alpha,2}(t+\Delta) = \int_{\tau}^{t+\Delta} \mathrm{d}\bar{t}\, e^{-iV_\alpha(t+\Delta-\bar{t})}\Lambda_\alpha(t+\Delta-\bar{t})G^0(t+\Delta-\bar{t}) \tag{S.2.15}$$

$$= \int_{\tau-\Delta}^{t} \mathrm{d}y e^{-iV_\alpha(t-y)}\Lambda_\alpha(t-y)G^0(t-y) \tag{S.2.16}$$

$$= I_{\alpha,2}(t) + \int_{\tau-\Delta}^{\tau} \mathrm{d}y e^{-iV_\alpha(t-y)}\Lambda_\alpha(t-y)G^0(t-y) \tag{S.2.17}$$

$$\approx I_{\alpha,2}(t) + \frac{\Delta}{2}\Big[e^{-iV_\alpha(t-\tau+\Delta)}\Lambda_\alpha(t-\tau+\Delta)G^0(t-\tau+\Delta) \tag{S.2.18}$$

$$+ e^{-iV_\alpha(t-\tau)}\Lambda_\alpha(t-\tau)G^0(t-\tau)\Big] \tag{S.2.19}$$

This integral requires the GF $G^0(t-\tau)$ which we are already computing.

3 Laser used

To analyze Laser we use Peierls substitution and since the system is finite we need to include the electric potential ϕ

$$H_s(t) = \sum_{\langle ij\rangle} e^{i\theta_{ij}} c^\dagger_{i\sigma}(-t_s\mathbb{I} + \boldsymbol{\alpha}_{ij}\cdot\boldsymbol{\tau})_{\sigma\sigma'}c_{j\sigma'} + \sum_{i\sigma}\epsilon_{i\sigma}(t)\hat{n}_{i\sigma} - \mathbf{B}\cdot\sum_i \hat{\mathbf{s}}_i, \tag{S.3.1}$$

$$H_{s-d} = -g\sum_i \hat{\mathbf{s}}_i\cdot\hat{\mathbf{S}}_i, \tag{S.3.2}$$

$$H_d = \sum_{\langle ij\rangle}\Big[J\hat{\mathbf{S}}_i\cdot\hat{\mathbf{S}}_j + \mathbf{D}_{ij}\cdot\hat{\mathbf{S}}_i\times\hat{\mathbf{S}}_j\Big] - \mathbf{B}\cdot\sum_i\hat{\mathbf{S}}_i - K\sum_i\hat{S}^2_{i,z}. \tag{S.3.3}$$

$$+\sum_{i\sigma}(i_x - i_{x,0})\phi c^\dagger_{i\sigma}c_{i\sigma}e^{-(i_x-i_{x,0})^2/(2\sigma^2)+(i_y-i_{y,0})^2/(2\sigma^2)} \tag{S.3.4}$$

$t_c = t_d = 45$,$A = 2$ i_x is the x-component of the index and $i_{x,0}$ is the center point in the lattice in x-direction.

$$f_x = \begin{cases} -i\sqrt{2}A\sin(\omega t)\sin^2(\pi t/(2t_c)) & t<t_c \\ -i\sqrt{2}A\sin(\omega t)\cos^2(\pi(t-t_d)/(2t_c)) & t<t_d+t_c \\ 0 & t_d+t_c<t \end{cases} \tag{S.3.5}$$

$$\phi = \begin{cases} -A0.06\sqrt{2}\cos(\omega t)\sin^2(\pi t/(2t_c)) & t<t_c \\ -A0.06\sqrt{2}\sin(\omega t)\cos^2(\pi(t-t_d)/(2t_c)) & t<t_d+t_c \\ 0 & t_d+t_c<t \end{cases} \tag{S.3.6}$$

θ_{ij} are the Peirels phases obtained by integrating over the Gaussian envelope-function and they are multiplied by f_x if the hopping is in x-direction otherwise they are zero. 0.06 is a constant which arises due to us choosing a near infrared laser. For more information see [2].